Applications of quantum Monte Carlo methods in condensed systems

Jindřich Kolorenč

Institute of Physics, Academy of Sciences of the Czech Republic, Na Slovance 2, 18221 Praha 8, Czech Republic

I. Institut für Theoretische Physik, Universität Hamburg, Jungiusstraße 9, 20355 Hamburg, Germany

kolorenc@fzu.cz

Lubos Mitas

Department of Physics and Center for High Performance Simulation, North Carolina State University, Raleigh, North Carolina 27695, USA

lmitas@unity.ncsu.edu

arXiv:1010.4992v1 [physics.comp-ph] 24 Oct 2010

The quantum Monte Carlo methods represent a powerful and broadly applicable computational tool for finding very accurate solutions of the stationary Schrödinger equation for atoms, molecules, solids and a variety of model systems. The algorithms are intrinsically parallel and are able to take full advantage of the present-day high-performance computing systems. This review article concentrates on the fixed-node/fixed-phase diffusion Monte Carlo method with emphasis on its applications to electronic structure of solids and other extended many-particle systems.

PACS numbers: 02.70.Ss, 71.15.−m, 31.15.−p

To appear in *Rep. Prog. Phys.*

1 Introduction **1**
1.1 Many-body stationary Schrödinger equation . . . 3

2 Methods **4**
2.1 Variational Monte Carlo . . . 4
2.2 Diffusion Monte Carlo . . . 5
2.2.1 Fixed-node/fixed-phase approximation . . 6
2.2.2 Sampling the probability distribution . . 6
2.2.3 General expectation values . . . 9
2.2.4 Spin degrees of freedom . . . 9
2.3 Pseudopotentials . . . 9

3 From a finite supercell to the thermodynamic limit **10**
3.1 Twist-averaged boundary conditions . . . 11
3.2 Ewald formula . . . 12
3.3 Extrapolation to the thermodynamic limit . . . 13
3.4 An alternative model for Coulomb interaction energy . . . 14

4 Trial wave functions **15**
4.1 Elementary properties . . . 15
4.2 Jastrow factor . . . 16
4.3 Slater–Jastrow wave function . . . 16
4.4 Antisymmetric forms with pair correlations . . . 18
4.5 Backflow coordinates . . . 18

5 Applications **19**
5.1 Properties of the homogeneous electron gas . . . 19
5.2 Cohesive energies of solids . . . 20
5.3 Equations of state . . . 21
5.4 Phase transitions . . . 22
5.5 Lattice defects . . . 23
5.6 Surface phenomena . . . 23
5.7 Excited states . . . 24
5.8 BCS–BEC crossover . . . 25

6 Concluding remarks **26**

1 Introduction

Many properties of condensed matter systems can be calculated from solutions of the stationary Schrödinger equation describing interacting ions and electrons. The grand challenge of solving the Schrödinger equation has been around from the dawn of quantum mechanics and remains at the forefront of the condensed matter physics today and, undoubtedly, for many decades to come.

The task of solving the Schrödinger equation for systems of electrons and ions, and predicting the quantities of interest such as cohesion and binding energies, electronic gaps, crystal structures, variety of magnetic phases or formation of quantum condensates is nothing short of formidable. Paul Dirac recognized this state of affairs already in 1929: "The general theory of quantum mechanics is now almost complete ... The underlying physical laws necessary for the mathemat-

ical theory of a large part of physics and the whole chemistry are thus completely known, and the difficulty is only that the exact application of these laws leads to equations much too complicated to be soluble." [1] Arguably, this is the most fundamental approach to the physics of condensed matter: Applications of the rigorous quantum laws to models that are as close to reality as currently feasible.

The goal of finding accurate solutions for stationary quantum states is hampered by a number of difficulties inherent to many-body quantum systems:

(i) Even moderately sized model systems contain anywhere between tens to thousands of quantum particles. Moreover, we are often interested in expectation values in the thermodynamic limit that is usually reached by extrapolations from finite sizes. Such procedures typically require detailed information about the scaling of the quantities of interest with the system size.

(ii) Quantum particles interact and the interactions affect the nature of quantum states. In many cases, the influence is profound.

(iii) The solutions have to conform to quantum symmetries such as the fermionic antisymmetry linked to the Pauli exclusion principle. This is a fundamental departure from classical systems and poses different challenges which call for new analytical ideas and computational strategies.

(iv) For meaningful comparisons with experiments, the required accuracy is exceedingly high, especially when comparing with precise data from spectroscopic and low-temperature studies.

In the past, the most successful approaches to address these challenges were based mostly on reductionist ideas. The problem is divided into the dominant effects, which are treated explicitly, and the rest, which is then dealt with by approximate methods based on variety of analytical tools: perturbation expansions, mean-field methods, approximate transformations to known solutions, and so on. The reductionist approaches have been gradually developed into a high level of sophistication and despite their limitations, they are still the most commonly used strategies in many-body physics.

The progress in computer technology has opened a new avenue for studies of quantum (and many other) problems and has enabled researchers to obtain results beyond the scope of analytic many-body theories. The performance of current large computers makes computational investigations of many-body quantum systems viable, allowing predictions that would be difficult or impossible to make otherwise. The quantum Monte Carlo (QMC) methods described in this review provide an interesting illustration of what is currently possible and how much the computational methods can enrich and make more precise our understanding of the quantum world.

Some of the ideas used in QMC methods go back to the times before the invention of electronic computers. Already in 1930s Enrico Fermi noticed similarities between the imaginary time Schrödinger equation and the laws governing stochastic processes in statistical mechanics. In addition, based on memories of his collaborator Emilio Segrè, Fermi also envisioned stochastic methodologies for solving the Schrödinger equation, which were very similar to concepts developed decades later. These Fermi's ideas were acknowledged by Metropolis and Ulam in a paper from 1949 [2], where they outlined a stochastic approach to solving various physical problems and discussed merits of "modern" computers for its implementation. In fact, this group of scientists at the Los Alamos National Laboratory attempted to calculate the hydrogen molecule by a simple version of QMC in the early 1950s, around the same time when a pioneering work on the first Monte Carlo study of classical systems was published by Metropolis and coworkers [3]. In the late 1950s, Kalos initiated development of QMC simulations and methodologies for few-particle systems and laid down the statistical and mathematical foundations of the Green's function Monte Carlo method [4]. Eventually, simulations of large many-particle systems became practicable as well. First came studies of bosonic fluids modelling ^{4}He [5–7], and later followed investigations of extended fermionic systems exemplified by liquid ^{3}He [8, 9] and by the homogeneous electron gas [10, 11]. Besides these applications to condensed matter, essentially the same methods were in mid-seventies introduced in quantum chemistry to study small molecular systems [12, 13]. To date, various QMC methods were developed and applied to the electronic structure of atoms, molecules and solids, to quantum lattice models, as well as to nuclear and other systems with contributions from many scientists.

The term "quantum Monte Carlo" covers several related stochastic methodologies adapted to determine ground-state, excited-state or finite-temperature equilibrium properties of a variety of quantum systems. The word "quantum" is important since QMC approaches differ significantly from Monte Carlo methods for classical systems. For an overview of the latter see for instance [14]. QMC is not only a computational tool for large-scale problems, but it also encompasses a

substantial amount of analytical work needed to make such calculations feasible. QMC simulations often utilize results of the more traditional electronic structure methods in order to increase efficiency of the calculations. These ingredients are combined to optimally balance the computational cost with achieved accuracy. The key point for gaining new insights is an appropriate analysis of the quantum states and associated many-body effects. It is typically approached iteratively: Simulations indicate the gaps in understanding of the physics, closing these gaps is subsequently attempted and the improvements are assessed in the next round. Such a process involves construction of zero- or first-order approximations for the desired quantum states, incorporation of new analytical insights, and development of new numerical algorithms.

QMC methods inherently incorporate several types of internal checks, and many of the algorithms used possess various rigorous bounds, such as the variational property of the total energy. Nevertheless, the coding and numerical aspects of the simulations are not entirely error-proof and the obtained results should be verified independently. Indeed, it is a part of the modern computational-science practice that several groups revisit the same problem with independent software packages and confirm or challenge the results. "Biodiversity" of the available QMC codes on the scientific market (including QWalk [15], QMCPACK [16], CHAMP [17], CASINO [18], QMcBeaver [19] and others) provides the important alternatives to verify the algorithms and their implementations. This is clearly a rather labourious, slow and tedious process, nevertheless, experience shows that independently calculated results and predictions eventually reach a consensus and such verified data become widely used standards.

In this overview we present QMC methods that solve the stationary Schrödinger equation for condensed systems of interacting fermions in continuous space. Conceptually very straightforward is the variational Monte Carlo (VMC) method, which builds on explicit construction of *trial (variational) wave functions* using stochastic integration and parameter optimization techniques. More advanced approaches represented by the diffusion Monte Carlo (DMC) method are based on projection operators that find the ground state within a given symmetry class. Practical versions of the DMC method for a large number of particles require dealing with the well-known fermion sign problem originating in the antisymmetry of the fermionic wave functions. The most commonly used approach to overcome this fundamental obstacle is the fixed-node approximation. This approximation introduces the so-called *fixed-node error*, which appears to be the key limiting factor in further increase in accuracy. As we will see in section 5, the fixed-node error is typically rather small and does not hinder calculation of robust quantities such as cohesion, electronic gaps, optical excitations, defect energies or potential barriers between structural conformations. By robust we mean quantities which are of the order of tenths of an electronvolt to several electronvolts. Nevertheless, the fixed-node errors can bias results for more subtle phenomena, such as magnetic ordering or effects related to superconductivity. Development of strategies to alleviate such biases is an active area of research.

Fixed-node DMC simulations are computationally rather demanding when compared to the mainstream electronic structure methods that rely on mean-field treatment of electron-electron interactions. On the other hand, QMC calculations can provide unique insights into the nature of quantum phenomena and can verify many theoretical ideas. As such, they can produce not only accurate numbers but also new understanding. Indeed, QMC methodology is very much an example of "it from bit" paradigm, alongside, for example, the substantial computational efforts in quantum chromodynamics, which not only predict hadron masses but also contribute to the validation of the fundamental theory [20, 21]. Just a few decades ago it was difficult to imagine that one would be able to solve the Schrödinger equation for hundreds of electrons by means of an explicit construction of the many-body wave function. Today, such calculations are feasible using available computational resources. At the same time, there remains more to be done to make the methods more insightful, more efficient, and their application less labourious. We hope that this review will contribute to the growing interest in this rapidly developing field of research.

The review is organized as follows: The remainder of this section provides mostly definitions and notations. Section 2 follows with description of the VMC and DMC methods. The strategies for calculation of quantities in the thermodynamic limit are presented in section 3. Section 4 introduces currently used forms of the trial wave functions and their recently developed generalizations. The overview of applications presented in section 5 is focused on QMC calculations of a variety of solids and related topics.

1.1 Many-body stationary Schrödinger equation

Let us consider a system of quantum particles such as electrons and ions interacting via Coulomb potentials. Since the masses of nuclei and electrons differ by three orders of magnitude or more, the problem can be sim-

plified with the aid of the *Born–Oppenheimer approximation*, which separates the electronic degrees of freedom from the slowly moving system of ions. The electronic part of the non-relativistic Born–Oppenheimer hamiltonian is given by

$$\hat{H} = -\frac{1}{2}\sum_i \nabla_i^2 - \sum_{i,I} \frac{Z_I}{|\boldsymbol{r}_i - \boldsymbol{x}_I|} + \sum_{j<i} \frac{1}{|\boldsymbol{r}_i - \boldsymbol{r}_j|}\,, \quad (1)$$

where i and j label the electrons and I runs over the ions with charges Z_I. Throughout the review we employ the atomic units, $m_\mathrm{e} = \hbar = e = 4\pi\varepsilon_0 = 1$, where m_e is the electron mass, $-e$ is the electron charge and ε_0 is the permittivity of a vacuum. We are interested in eigenstates $|\Psi_n\rangle$ of the stationary Schrödinger equation

$$\hat{H}|\Psi_n\rangle = E_n|\Psi_n\rangle\,. \quad (2)$$

Colloquially, we call such solutions (either exact or approximate) and derived properties collectively the electronic structure.

An important step forward in calculations of the eigenstates was made by Hartree [22] and Fock [23] by establishing the simplest antisymmetric wave functions and by formulating the Hartree–Fock (HF) theory, which correctly takes into account the Pauli *exclusion principle* [24, 25]. The HF theory replaces the hard problem of many interacting electrons with a system of independent particles in an effective, self-consistent field. The theory was further developed by Slater [26] and others, and it has become a starting point of many sophisticated approaches to fermionic many-body problems.

For periodic systems, the effective free-electron theory and the *band theory* of Bloch [27] were the first crucial steps towards our present understanding of the real crystals. In 1930s, Wigner and Seitz [28, 29] performed the first quantitative calculations of the electronic states in sodium metal. Building upon the homogeneous electron gas model, the density-functional theory (DFT) was invented by Hohenberg and Kohn [30] and further developed by Kohn and Sham [31] who formulated the local density approximation (LDA) for the exchange-correlation functional. These ideas were later elaborated by including spin polarization [32], by constructing the generalized gradient approximation (GGA) [33, 34], and by designing a variety of orbital-dependent exchange-correlation functionals [35–37]. The DFT has proved to be very successful and has become the mainstream computational method for many applications, which cover not only solids but also molecules and even nuclear and other systems [38, 39]. The density-functional theory together with the Hartree–Fock and post-Hartree–Fock methods [40] are relevant for our discussion of quantum Monte Carlo methodology, since the latter uses the results of these approaches as a reference and also for construction of the many-body wave functions. Familiarity with the basic concepts of the Hartree–Fock and density-functional theories is likely to make the subsequent sections easier to follow, but we believe that it is not a necessary prerequisite for understanding our exposition of the QMC methods and their foundations.

2 Methods

2.1 Variational Monte Carlo

In the variational Monte Carlo method, the ground state of a hamiltonian $\hat{H}$ is approximated by some trial wave function $|\Psi_\mathrm{T}\rangle$, whose form is chosen following a prior analysis of the physical system being investigated. Functional forms relevant to solid-state applications will be discussed later in section 4. Typically a number of parameters are introduced into $|\Psi_\mathrm{T}\rangle$, and these parameters are varied to minimize the expectation value $E_{\Psi_\mathrm{T}^2} = \langle\Psi_\mathrm{T}|\hat{H}|\Psi_\mathrm{T}\rangle/\langle\Psi_\mathrm{T}|\Psi_\mathrm{T}\rangle$ in order to bring the trial wave function as close as possible to the actual ground state $|\Psi_0\rangle$.

Wave functions of interacting systems are non-separable, and the integration needed to evaluate $E_{\Psi_\mathrm{T}^2}$ is therefore a difficult task. Although it is possible to write these wave functions as linear combinations of separable terms, this tactic is viable only for a limited number of particles, since the length of such expansions grows very quickly as the system size increases. The variational Monte Carlo method employs a stochastic integration that can treat the non-separable wave functions directly. The expectation value $E_{\Psi_\mathrm{T}^2}$ is written as

$$E_{\Psi_\mathrm{T}^2} = \int \frac{|\Psi_\mathrm{T}(\mathcal{R})|^2}{\langle\Psi_\mathrm{T}|\Psi_\mathrm{T}\rangle} \frac{\big[\hat{H}\Psi_\mathrm{T}\big](\mathcal{R})}{\Psi_\mathrm{T}(\mathcal{R})}\,\mathrm{d}^{3N}\mathcal{R} \approx E_\mathrm{VMC} = \frac{1}{\mathcal{N}}\sum_{i=1}^{\mathcal{N}} \frac{\big[\hat{H}\Psi_\mathrm{T}\big](\mathcal{R}_i)}{\Psi_\mathrm{T}(\mathcal{R}_i)}\,, \quad (3)$$

where $\mathcal{R} = (\boldsymbol{r}_1, \boldsymbol{r}_2, \ldots, \boldsymbol{r}_N)$ is a $3N$-dimensional vector encompassing the coordinates of all N particles in the system and the sum runs over $\mathcal{N}$ such vectors $\{\mathcal{R}_i\}$ sampled from the multivariate probability density $\rho(\mathcal{R}) = |\Psi_\mathrm{T}(\mathcal{R})|^2/\langle\Psi_\mathrm{T}|\Psi_\mathrm{T}\rangle$. The summand $E_\mathrm{L}(\mathcal{R}) = \big[\hat{H}\Psi_\mathrm{T}\big](\mathcal{R})/\Psi_\mathrm{T}(\mathcal{R})$ is usually referred to as the local energy. We assume spin-independent hamiltonians, and therefore spin variables do not explicitly enter the evaluation of the expectation value (3). This statement is further corroborated in section 4.1 where the elementary properties of the trial wave functions $|\Psi_\mathrm{T}\rangle$ are discussed.

Equation (3) transforms the multidimensional integration into a problem of sampling a complicated probability distribution. The samples $\{\mathcal{R}_i\}$ can be obtained such that they constitute a Markov chain with transitions $\mathcal{R}_{i+1} \leftarrow \mathcal{R}_i$ governed by a stochastic matrix $M(\mathcal{R}_{i+1} \leftarrow \mathcal{R}_i)$ whose stationary distribution coincides with the desired probability density $\rho(\mathcal{R})$,

$$\rho(\mathcal{R}') = \int M(\mathcal{R}' \leftarrow \mathcal{R})\rho(\mathcal{R})\,\mathrm{d}^{3N}\mathcal{R} \quad \text{for all } \mathcal{R}'. \quad (4)$$

After a period of equilibration, the members of the Markov sequence sample the stationary distribution regardless of the starting point of the chain, provided the matrix $M(\mathcal{R}' \leftarrow \mathcal{R})$ is ergodic. Inspired by the way the samples explore the configuration space, they are often referred to as walkers.

The Markov chain can be conveniently constructed with the aid of the Metropolis method [3, 41]. The transition matrix is factorized into two parts, $M(\mathcal{R}' \leftarrow \mathcal{R}_i) = T(\mathcal{R}' \leftarrow \mathcal{R}_i)A(\mathcal{R}' \leftarrow \mathcal{R}_i)$, which correspond to two consecutive stochastic processes: A candidate $\mathcal{R}'$ for $(i+1)$-th sample is proposed according to the probability $T(\mathcal{R}' \leftarrow \mathcal{R}_i)$ and this move is then either accepted with the probability $A(\mathcal{R}' \leftarrow \mathcal{R}_i)$ or rejected with the probability $1 - A(\mathcal{R}' \leftarrow \mathcal{R}_i)$. If the move is accepted, the new member of the sequence is $\mathcal{R}_{i+1} = \mathcal{R}'$, otherwise it is $\mathcal{R}_{i+1} = \mathcal{R}_i$. The length of the chain is thus incremented in either case. The acceptance probability $A(\mathcal{R}' \leftarrow \mathcal{R}_i)$, complementing some given $T(\mathcal{R}' \leftarrow \mathcal{R}_i)$ and $\rho(\mathcal{R})$ such that the stationarity condition (4) is fulfilled, is not unique. The choice corresponding to the Metropolis algorithm reads

$$A(\mathcal{R}' \leftarrow \mathcal{R}) = \min\left[1, \frac{T(\mathcal{R} \leftarrow \mathcal{R}')\,\rho(\mathcal{R}')}{T(\mathcal{R}' \leftarrow \mathcal{R})\,\rho(\mathcal{R})}\right] \quad (5)$$

and depends only on ratios of T and ρ. Consequently, normalization of the trial wave function $|\Psi_\mathrm{T}\rangle$ is completely irrelevant for the Monte Carlo evaluation of the quantum-mechanical expectation values. The freedom to choose the proposal probability $T(\mathcal{R}' \leftarrow \mathcal{R}_i)$ can be exploited to improve ergodicity of the sampling, for instance, to make it easier to overcome a barrier of low probability density ρ separating two high-density regions. A generic choice for $T(\mathcal{R}' \leftarrow \mathcal{R}_i)$ is a Gaussian distribution centered at $\mathcal{R}_i$ with its width tuned to optimize the efficiency of the sampling.

The variational energy E_VMC is a stochastic variable, and an appropriate characterization of the random error $E_\mathrm{VMC} - E_{\Psi_\mathrm{T}^2}$ is thus an integral part of the variational Monte Carlo method. When the sampled local energies $E_\mathrm{L}(\mathcal{R}_i)$ are sufficiently well behaved [42], this error can be represented by the variance of E_VMC. In such cases, the error scales as $\mathcal{N}^{-1/2}$ and is proportional to fluctuations of the local energy. Reliable estimation of the variance of E_VMC is a non-trivial affair since the random samples $\{\mathcal{R}_i\}$ generated by means of the Markov chain are correlated. These correlations are not known *a priori* and depend on the particular form of the transition matrix M that varies from case to case. Nevertheless, it is possible to estimate the variance without detailed knowledge of the correlation properties of the chain with the aid of the so-called blocking method [43].

The fluctuations of the local energy E_L are reduced as the trial wave function $|\Psi_\mathrm{T}\rangle$ approaches an eigenstate of the hamiltonian, and E_L becomes a constant when $|\Psi_\mathrm{T}\rangle$ is an eigenstate. In particular, it is crucial to remove as many singularities from E_L as possible by a proper choice of the trial function. Section 4.1 illustrates how it is achieved in the case of the Coulomb potential that is singular at particle coincidences.

The total energy is not the only quantity of interest and evaluation of other ground-state expectation values is often desired. The formalism sketched so far remains unchanged, only the local energy is replaced by a local quantity $A_\mathrm{L}(\mathcal{R}) = \big[\hat{A}\Psi_\mathrm{T}\big](\mathcal{R})/\Psi_\mathrm{T}(\mathcal{R})$ corresponding to a general operator $\hat{A}$. An important difference between A_L and the local energy is that fluctuations of A_L do not vanish when $|\Psi_\mathrm{T}\rangle$ is an eigenstate of $\hat{H}$. These fluctuations can severely impact the efficiency of the Monte Carlo integration in $\langle\Psi_\mathrm{T}|\hat{A}|\Psi_\mathrm{T}\rangle/\langle\Psi_\mathrm{T}|\Psi_\mathrm{T}\rangle$, and the random error can decay even slower than $\mathcal{N}^{-1/2}$ [42]. The trial wave function cannot be altered to suppress the fluctuations in this case, but a modified operator $\hat{A}'$ can often be constructed such that $\langle\Psi_\mathrm{T}|\hat{A}'|\Psi_\mathrm{T}\rangle = \langle\Psi_\mathrm{T}|\hat{A}|\Psi_\mathrm{T}\rangle$ while the fluctuations of A_L are substantially reduced [44–48].

2.2 Diffusion Monte Carlo

The accuracy of the variational Monte Carlo method is limited by the quality of the trial wave function $|\Psi_\mathrm{T}\rangle$. This limitation can be overcome with the aid of the projector methods. In particular, the diffusion Monte Carlo method [12, 49–51] employs an imaginary time evolution

$$|\Psi_\mathrm{D}(t)\rangle = \exp\Big(-\big[\hat{H} - E_\mathrm{T}(t)\big]t\Big)\,|\Psi_\mathrm{T}\rangle\,, \quad (6)$$

where the energy offset E_T is introduced to maintain the wave-function norm at a fixed value. Formal properties of (6) can be elucidated by expanding the trial function $|\Psi_\mathrm{T}\rangle$ in terms of the hamiltonian eigen-

states (2), which readily yields

$$|\Psi_{\mathrm{D}}(t)\rangle = \exp\Big(-\big[E_0 - E_{\mathrm{T}}(t)\big]t\Big)\Bigg[|\Psi_0\rangle\langle\Psi_0|\Psi_T\rangle + \sum_{n=1}^{\infty} \mathrm{e}^{-(E_n-E_0)t}|\Psi_n\rangle\langle\Psi_n|\Psi_T\rangle\Bigg]. \quad (7)$$

The ground state $|\Psi_0\rangle$ is indeed reached in the limit of large t as long as the trial function was not orthogonal to $|\Psi_0\rangle$ from the beginning. The requirement of a finite norm of $|\Psi_{\mathrm{D}}(t)\rangle$ translates into a formula

$$E_0 = \lim_{t\to\infty} E_{\mathrm{T}}(t) \quad (8)$$

that can be used to obtain the ground-state energy. An alternative approach is to evaluate the matrix element $E_{\Psi_{\mathrm{D}}\Psi_{\mathrm{T}}} = \langle\Psi_{\mathrm{D}}(t)|\hat{H}|\Psi_{\mathrm{T}}\rangle/\langle\Psi_{\mathrm{D}}(t)|\Psi_{\mathrm{T}}\rangle$ that asymptotically coincides with the ground-state energy, since $\langle\Psi_0|\hat{H}|\Psi_T\rangle/\langle\Psi_0|\Psi_T\rangle = \langle\Psi_0|\hat{H}|\Psi_0\rangle/\langle\Psi_0|\Psi_0\rangle$. The integration in $E_{\Psi_{\mathrm{D}}\Psi_{\mathrm{T}}}$ can be performed stochastically in analogy with the VMC method,

$$E_{\Psi_{\mathrm{D}}\Psi_{\mathrm{T}}} = \int \frac{\Psi^*_{\mathrm{D}}(\mathcal{R},t)\Psi_{\mathrm{T}}(\mathcal{R})}{\langle\Psi_{\mathrm{D}}(t)|\Psi_{\mathrm{T}}\rangle} \frac{\big[\hat{H}\Psi_{\mathrm{T}}\big](\mathcal{R})}{\Psi_{\mathrm{T}}(\mathcal{R})}\,\mathrm{d}^{3N}\mathcal{R} \approx E_{\mathrm{DMC}} = \frac{1}{\mathcal{N}}\sum_{i=1}^{\mathcal{N}} E_{\mathrm{L}}(\mathcal{R}_i)\,, \quad (9)$$

where the individual samples $\mathcal{R}_i$ are now drawn from a probability distribution defined as $\rho(\mathcal{R},t) = \Psi^*_{\mathrm{D}}(\mathcal{R},t)\Psi_{\mathrm{T}}(\mathcal{R})/\langle\Psi_{\mathrm{D}}(t)|\Psi_{\mathrm{T}}\rangle$.

2.2.1 Fixed-node/fixed-phase approximation

The Monte Carlo integration indicated in (9) is possible only if $\rho(\mathcal{R},t)$ is real-valued and positive. Since the hamiltonians we usually deal with are symmetric with respect to time reversal, the eigenfunctions can be chosen real. Unfortunately, many-electron wave functions must necessarily have alternating sign to comply with the fermionic antisymmetry. In general, the initial guess $|\Psi_{\mathrm{T}}\rangle$ will have different plus and minus sign domains (also referred to as nodal pockets or nodal cells) than the sought for ground-state wave function $|\Psi_0\rangle$, which results in changing sign of $\rho(\mathcal{R},t)$. In certain special cases, the correct sign structure of the ground state can be deduced from symmetry considerations [52–54], but in a general interacting system the exact position of the boundary between the positive and negative domains (the so-called fermionic node) is unknown and is determined by the quantum many-body physics [55]. A number of exact properties of the fermionic nodes have been discovered [56–59], but a lot remains to be done in order to transform this knowledge into constructive algorithms for the trial wave functions.

The problem with the variable sign of $\rho(\mathcal{R},t)$ can be circumvented by complementing the projection (6) with the so-called fixed-node constraint [13],

$$\Psi_{\mathrm{D}}(\mathcal{R},t)\Psi_{\mathrm{T}}(\mathcal{R}) \geq 0 \quad \text{for all } \mathcal{R} \text{ and all } t\,. \quad (10)$$

Doing so, $\lim_{t\to\infty}|\Psi_{\mathrm{D}}(t)\rangle$ only approximates $|\Psi_0\rangle$, since the projection cannot entirely reach the ground state if the initial wave function $|\Psi_{\mathrm{T}}\rangle$ does not possess the exact nodes. The total energy calculated with this fixed-node method represents an upper-bound estimate of the true ground-state energy because the projection (6) is restricted to a subspace of the whole Hilbert space when the constraint (10) is implemented [60–62]. The fixed-node approximation has proved very fruitful in quantum chemistry [63, 64] as well as for investigation of the electronic structure of solids as testified by the applications reviewed in section 5.

In calculations of extended systems and especially metals, it is beneficial to allow for boundary conditions that break the time-reversal symmetry, since it facilitates reduction of finite-size effects (section 3.1). The eigenfunctions are then complex-valued and a generalization of the fixed-node approximation is required. The constraint (10) is replaced with $\Psi_{\mathrm{D}}(t) = |\Psi_{\mathrm{D}}(t)|\,\mathrm{e}^{\mathrm{i}\varphi_{\mathrm{T}}}$, where φ_{T} is the phase of the trial wave function $\Psi_{\mathrm{T}} = |\Psi_{\mathrm{T}}|\,\mathrm{e}^{\mathrm{i}\varphi_{\mathrm{T}}}$ [65]. The phase φ_{T} is held constant during the DMC simulation to guarantee that $\rho(\mathcal{R},t)$ stays non-negative for all $\mathcal{R}$ and t. Additionally, a complex trial wave function $|\Psi_{\mathrm{T}}\rangle$ causes the local energy E_{L} to be complex as well. The appropriate modification of the estimate for the total energy (9) coinciding with the asymptotic value of $E_{\mathrm{T}}(t)$ then reads

$$E_{\mathrm{DMC}} = \frac{1}{\mathcal{N}}\sum_{i=1}^{\mathcal{N}} \mathrm{Re}\big[E_{\mathrm{L}}(\mathcal{R}_i)\big]\,. \quad (11)$$

Analogous to the fixed-node approximation, the fixed-phase method provides a variational upper-bound estimate of the true ground-state energy. Moreover, the fixed-phase approximation reduces to the fixed-node approximation when applied to real-valued wave functions.

2.2.2 Sampling the probability distribution

The unnormalized probability distribution that we wish to sample in the fixed-phase DMC method,

$$f(\mathcal{R},t) = \Psi^*_{\mathrm{D}}(\mathcal{R},t)\Psi_{\mathrm{T}}(\mathcal{R}) = |\Psi_{\mathrm{D}}(\mathcal{R},t)||\Psi_{\mathrm{T}}(\mathcal{R})|\,, \quad (12)$$

referred to as the mixed distribution, fulfills an equation of motion

$$
\begin{aligned}
-\partial_t f(\mathcal{R},t) = \\
&-\frac{1}{2}\nabla^2 f(\mathcal{R},t) + \nabla\cdot\big[\boldsymbol{v}_\mathrm{D}(\mathcal{R}) f(\mathcal{R},t)\big] \\
&+ f(\mathcal{R},t)\Big[\mathrm{Re}\big[E_\mathrm{L}(\mathcal{R})\big] - (1+t\,\partial_t)E_\mathrm{T}(t)\Big] \quad (13)
\end{aligned}
$$

that is derived by differentiating (6) and (12) with respect to time, combining the resulting expressions and rearranging the terms. The drift velocity $\boldsymbol{v}_\mathrm{D}$ introduced in (13) is defined as $\boldsymbol{v}_\mathrm{D} = \nabla \ln|\Psi_\mathrm{T}|$ and ∇ denotes the $3N$-dimensional gradient with respect to $\mathcal{R}$. The equation of motion is valid in this form only as long as the kinetic energy is the sole non-local operator in the hamiltonian. Strategies for inclusion of non-local pseudopotentials will be discussed later in section 2.3. The case of the fixed-node approximation is virtually identical to (13), except that the local energy is real by itself. The following discussion therefore applies to both methods.

The time evolution of the mixed distribution $f(\mathcal{R},t)$ can be written in the form of a convolution

$$
f(\mathcal{R},t) = \int G(\mathcal{R}\leftarrow\mathcal{R}',t) f(\mathcal{R}',0)\,\mathrm{d}^{3N}\mathcal{R}' \,, \qquad (14)
$$

where $f(\mathcal{R},0) = |\Psi_\mathrm{T}(\mathcal{R})|^2$ and the Green's function $G(\mathcal{R}\leftarrow\mathcal{R}',t) = \langle\mathcal{R}|\hat{G}(t)|\mathcal{R}'\rangle$ is a solution of (13) with the initial condition $G(\mathcal{R}\leftarrow\mathcal{R}',0) = \delta(\mathcal{R}-\mathcal{R}')$. Making use of the Trotter–Suzuki formula [66, 67], the Green's function is approximated by a product of short-time expressions,

$$
\hat{G}(t) = \underbrace{\big[\hat{G}_\mathrm{g/d}(\tau)\,\hat{G}_\mathrm{diff}(\tau)\,\hat{G}_\mathrm{drift}(\tau)\big]}_{\hat{G}_\mathrm{st}(\tau)}{}^{M} + \mathrm{O}(\tau)\,, \quad (15)
$$

where τ denotes t/M and the exact solution of (13) is approached as this time step goes to zero. Consequently, the DMC simulations should be repeated for several sizes of the time step and an extrapolation of the results to $\tau\to 0$ should be performed in the end. For simplicity, we show in (15) only the simplest Trotter–Suzuki decomposition which has a time step error proportional to τ. Commonly used are higher order approximations whose errors scale as τ^2 or τ^3. The three new Green's functions constituting the short-time approximation $\hat{G}_\mathrm{st}$ can be explicitly written as

$$
\begin{aligned}
&G_\mathrm{drift}(\mathcal{R}\leftarrow\mathcal{R}',\tau) \qquad (16)\\
&\quad = \big[1-\tau\nabla\cdot\boldsymbol{v}_\mathrm{D}(\mathcal{R}')\big]\delta\big[\mathcal{R}-\mathcal{R}'-\boldsymbol{v}_\mathrm{D}(\mathcal{R}')\tau\big] \\
&\qquad + \mathrm{O}(\tau^2)\,,
\end{aligned}
$$

$$
\begin{aligned}
&G_\mathrm{diff}(\mathcal{R}\leftarrow\mathcal{R}',\tau) \qquad (17)\\
&\quad = \frac{1}{(2\pi\tau)^{3N/2}}\exp\left[-\frac{(\mathcal{R}-\mathcal{R}')^2}{2\tau}\right],
\end{aligned}
$$

$$
\begin{aligned}
&G_\mathrm{g/d}(\mathcal{R}\leftarrow\mathcal{R}',\tau) \qquad (18)\\
&\quad = \exp\Big[-\tau\Big(\mathrm{Re}\big[E_\mathrm{L}(\mathcal{R})\big] - E_\mathrm{T}(t)\Big)\Big]\delta\big[\mathcal{R}-\mathcal{R}'\big]\,,
\end{aligned}
$$

and correspond to the three non-commuting operators from the right-hand side of (13) in the order: drift $\big(\nabla\cdot\big[\boldsymbol{v}_\mathrm{D}(\mathcal{R})\,\bullet\big]\big)$, diffusion $\big(-\nabla^2/2\,\bullet\big)$ and growth/decay $\big(\bullet\big[\mathrm{Re}[E_\mathrm{L}(\mathcal{R})] - (1+t\,\partial_t)E_\mathrm{T}(t)\big]\big)$. The drift and diffusion Green's functions preserve the normalization of $f(\mathcal{R},t)$ whereas the growth/decay process does not.

The factorization of the exact Green's function into the product of the short-time terms forms the basis of the stochastic process that represents the diffusion Monte Carlo algorithm. First, $\mathcal{M}$ samples $\{\mathcal{R}_i\}$ are drawn from the distribution $f(\mathcal{R},0) = |\Psi_\mathrm{T}(\mathcal{R})|^2$ just like in the VMC method. Subsequently, this set of walkers evolves such that it samples the mixed distribution $f(\mathcal{R},t)$ at any later time t. The probability distribution is updated from time t to $t+\tau$ by multiplication with the short-time Green's function,

$$
f(\mathcal{R},t+\tau) = \int G_\mathrm{st}(\mathcal{R}\leftarrow\mathcal{R}',\tau) f(\mathcal{R}',t)\,\mathrm{d}^{3N}\mathcal{R}' \,, \quad (19)
$$

which translates into the following procedure performed on each walker in the population:

(i) a drift move $\Delta\mathcal{R}_\mathrm{drift} = \boldsymbol{v}_\mathrm{D}(\mathcal{R}')\tau$ is proposed

(ii) a diffusion move $\Delta\mathcal{R}_\mathrm{diff} = \boldsymbol{\chi}$ is proposed, where $\boldsymbol{\chi}$ is a vector of Gaussian random numbers with variance τ and zero mean

(iii) the increment $\Delta\mathcal{R}_\mathrm{drift} + \Delta\mathcal{R}_\mathrm{diff}$ is accepted if it complies with the fixed-node condition $\Psi_\mathrm{T}(\mathcal{R}')\Psi_\mathrm{T}(\mathcal{R}'+\Delta\mathcal{R}_\mathrm{drift}+\Delta\mathcal{R}_\mathrm{diff}) > 0$, otherwise the walker stays at its original position; moves attempting to cross the node occur only due to inaccuracy of the approximate Green's function (15), and they vanish in the limit $\tau\to 0$; the moves $\Delta\mathcal{R}_\mathrm{drift}+\Delta\mathcal{R}_\mathrm{diff}$ are accepted without any constraint in the fixed-phase method

(iv) the growth/decay Green's function $G_\mathrm{g/d}$ is applied; several algorithms devised for this purpose are outlined in the following paragraph

(v) at this moment, the time step is finished and the simulation continues with another cycle starting back at (i).

After the projection period is completed, the algorithm samples the desired ground-state mixed distribution and the quantities needed for evaluation of various expectation values can be collected in step (v).

At this point we return to a more detailed discussion of several algorithmic representations of the growth/decay Green's function $G_{\mathrm{g/d}}$ needed in step (iv).

- The most straightforward way is to assign a weight w to each walker. These weights are set to 1 during the VMC initialization of the walker population and the application of $G_{\mathrm{g/d}}$ then amounts to a multiplication $w(t+\tau) = w(t)W(\mathcal{R})$, where the weighting factor is

$$W(\mathcal{R}) = \exp\Big[-\tau\Big(\mathrm{Re}\big[E_{\mathrm{L}}(\mathcal{R})\big] - E_{\mathrm{T}}(t)\Big)\Big]\,. \quad (20)$$

  Consequently, the formula for calculation of the total energy (11) is modified to

$$E_{\mathrm{DMC}} = \left(\sum_{i=1}^{\mathcal{N}} w_i\right)^{-1} \sum_{i=1}^{\mathcal{N}} w_i\, \mathrm{Re}\big[E_{\mathrm{L}}(\mathcal{R}_i)\big] \quad (21)$$

  and the walkers remain distributed according to $|\Psi_{\mathrm{T}}(\mathcal{R})|^2$ as in the VMC method. This algorithm is referred to as the *pure diffusion Monte Carlo* method [68, 69]. It is known to be intrinsically unstable at large projection times where the signal-to-noise ratio deteriorates [70], but it is still useful for small quantum-chemical systems [71–73].

- The standard DMC algorithm fixes the weights to $w = 1$ and instead allows for stochastically fluctuating size of the walker population by branching walkers in regions with large weighting factor $W(\mathcal{R})$ and by removing them from areas with small $W(\mathcal{R})$. The copies from high-probability regions are treated as independent samples in the subsequent time steps. The time dependence of the energy offset $E_{\mathrm{T}}(t)$ provides a population control mechanism that prevents the population from exploding or collapsing entirely [50, 74]. The *branching/elimination* algorithm is much more efficient in large many-body systems than the pure DMC method, although it also eventually reaches the limits of its applicability for a very large number of particles [75].

- An alternative to the fluctuating population are various flavours of the *stochastic reconfiguration* [15, 70, 76–78]. These algorithms complement each branched walker with high weighting factor $W(\mathcal{R})$ with one eliminated walker with small $W(\mathcal{R})$, and therefore the total number of walkers remains constant. This pairing introduces slight correlations into the walker population that are comparable to those caused by the population control feedback of the standard branching/elimination algorithm [75]. Keeping the population size fixed is advantageous for load balancing in parallel computational environments, since the number of walkers can be a multiple of the number of computer nodes (CPUs) at all times during the simulation.

The branching/elimination process interacts in a subtle way with the fixed-node constraint. Since the walkers are not allowed to cross the node, the branched and parent walkers always stay in the same nodal cell. If some of these cells are more favoured (that is, if they have a lower local energy on average), the walker population accumulates there and eventually vanishes from the less favoured cells. Such uneven distribution of samples would introduce a bias to the simulation. Fortunately, it does not happen, since all nodal cells of the ground-state wave functions are connected by particle permutations and are therefore equivalent, see the tiling theorem in [56]. For general excited states this theorem does not hold and the unwanted depopulation of some nodal cells can indeed be observed. The problem is absent from the fixed-phase method, since it contains no restriction on the walker propagation.

The branching/elimination algorithm is just one of the options of dealing with the weights along the stochastic paths. Another possibility was introduced by Baroni and Moroni as the so-called *reptation* algorithm [79], which recasts the sampling of both the path in the configuration space *and* the weight into a straightforward Monte Carlo process, avoiding thus some of the disadvantages of the DMC algorithm. The reptation method has its own sources of inefficiencies which can be, however, significantly alleviated [80].

This concludes our presentation of the stochastic techniques that are used to simulate the projection operator introduced in (6). We would like to bring to the reader's attention that the algorithm outlined in this section is rather rudimentary and illustrates only the general ideas. A number of important performance improvements are usually employed in practical simulations, see for instance [74] for further details.

2.2.3 General expectation values

So far, only the total energy was discussed in connection with the DMC method. An expression analogous to (9) can be written with any operator $\hat{A}$ in place of the hamiltonian $\hat{H}$. The acquired quantity $A_{\Psi_{\rm D}\Psi_{\rm T}} = \langle\Psi_{\rm D}|\hat{A}|\Psi_{\rm T}\rangle/\langle\Psi_{\rm D}|\Psi_{\rm T}\rangle$, called the mixed estimate, differs from the pure expectation value $\langle\Psi_{\rm D}|\hat{A}|\Psi_{\rm D}\rangle/\langle\Psi_{\rm D}|\Psi_{\rm D}\rangle$ unless $\hat{A}$ commutes with the hamiltonian. In general, the error is proportional to the difference between $|\Psi_D\rangle$ and $|\Psi_T\rangle$. The bias can be reduced to the next order using the following extrapolation [7, 50]

$$\frac{\langle\Psi_D|\hat{A}|\Psi_D\rangle}{\langle\Psi_D|\Psi_D\rangle} = 2\,\frac{\langle\Psi_D|\hat{A}|\Psi_T\rangle}{\langle\Psi_D|\Psi_T\rangle} - \frac{\langle\Psi_T|\hat{A}|\Psi_T\rangle}{\langle\Psi_T|\Psi_T\rangle} + \mathrm{O}\left(\left|\frac{\Psi_D}{\sqrt{\langle\Psi_D|\Psi_D\rangle}} - \frac{\Psi_T}{\sqrt{\langle\Psi_T|\Psi_T\rangle}}\right|^2\right). \quad (22)$$

Alternative methods that allow for a direct evaluation of the pure expectation values have been developed, such as the forward (or future) walking [50, 81, 82], the reptation quantum Monte Carlo [79, 83, 84], or the Hellman–Feynman operator sampling [85, 86]. Due to their certain limitations, these techniques do not fully replace the extrapolation (22)—they are usable only for local operators and the former two become computationally inefficient in large systems.

The discussion of the random errors from the end of section 2.1 applies also to the diffusion Monte Carlo method, except that the serial correlations among the data produced in the successive steps of the DMC simulations are typically larger than the correlations in the VMC data. Therefore, longer DMC runs are necessary to achieve equivalent suppression of the stochastic uncertainties of the calculated expectation values.

2.2.4 Spin degrees of freedom

The DMC method as outlined above samples only the spatial part of the wave function, and the spin degrees of freedom remain fixed during the whole simulation. This simplification follows from the assumption of a spin-independent hamiltonian that implies freezing of spins during the DMC projection (6). This is indeed the current state of the DMC methodology as applied to electronic-structure problems: In order to arrive at the correct spin state, a number of spin-restricted calculations are performed and the variational principle is employed to select the best ground state candidate among them.

Fixing spin variables is not possible for spin-dependent hamiltonians, such as for those containing spin-orbital interactions, since they lead to a non-trivial coupling of different spin configurations. In fact, spin-dependent quantum Monte Carlo methods were developed for studies of nuclear matter. A variant of the Green's function Monte Carlo method [87, 88] treats the spin degrees of freedom directly in their full state space. Since the number of spin configurations grows exponentially with the number of particles, this approach is limited to relatively small systems. More favourable scaling with the systems size offers the auxiliary field diffusion Monte Carlo method that samples the spin variables stochastically by means of auxiliary fields introduced via the Hubbard–Stratonovich transformation [89, 90]. Recently, a version of the auxiliary field DMC method was used to investigate properties of the two-dimensional electron gas in presence of the Rashba spin-orbital coupling [91].

2.3 Pseudopotentials

The computational cost of all-electron QMC calculations grows very rapidly with the atomic number Z of the elements constituting the simulated system. Theoretical analysis [92, 93] as well as practical calculations [94] indicate that the cost scales as $Z^{5.5-6.5}$. Most of the computer time spent in these simulations is used for sampling of large energy fluctuations in the core region, which have very little effect on typical properties of interest, such as interatomic bonding and low-energy excitations. For investigations of these quantities it is convenient to replace the core electrons with accurate pseudopotentials. A sizeable library of norm-conserving pseudopotentials targeted specifically to applications of the QMC methods has been built over the years [95–100].

Pseudopotentials substitute the ionic Coulomb potential with a modified expression,

$$-\frac{Z}{r} \quad \to \quad V(r) + \hat{W} \quad (23)$$

where $V(r)$ is a local term behaving asymptotically as $-(Z - Z_{\rm core})/r$ with $Z_{\rm core}$ being the number of eliminated core electrons. The operator $\hat{W}$ is non-local in the sense that electrons with different angular momenta experience different radial potentials. Explicitly, the matrix elements of the potential $\hat{W}$ associated with I-th atom in the system are

$$\langle\mathcal{R}|\hat{W}_I|\mathcal{R}'\rangle = \sum_i \sum_{l=0}^{l_{\max}} \sum_{m=-l}^{l} \langle\hat{\boldsymbol{r}}_{iI}|lm\rangle \times W_{I,l}(r_{iI})\delta(r_{iI} - r'_{iI})\langle lm|\hat{\boldsymbol{r}}'_{iI}\rangle\,, \quad (24)$$

where $|lm\rangle$ are angular momentum eigenstates, r_{iI} is the distance of an electron from the I-th nucleus and

$\hat{\boldsymbol{r}}_{iI}$ is the associated direction $\boldsymbol{r}_{iI}/r_{iI}$. Functions $W_{I,l}$ vanish for distances r_{iI} larger than some cut-off radius $r_{\rm c}$, and the sum $\sum_i$ therefore runs only over electrons that are sufficiently close to the particular nucleus.

Evaluation of pseudopotentials in the VMC method is straightforward, despite the fact that the local energy $E_{\rm L}$ itself involves integrals. As can be inferred from the form of the matrix elements (24), these are two-dimensional integrals over surfaces of spheres centered at the nuclei. The integration can be implemented with the aid of the Gaussian quadrature rules that employ favourably sparse meshes [101, 102].

The use of non-local pseudopotentials in the fixed-node DMC method is more involved, since the sampling algorithm outlined in section 2.2.2 explicitly assumed that all potentials were local. Non-local hamiltonian terms can be formally incorporated by introducing an extra member into the Trotter break-up (15), namely

$$\begin{aligned} &G_{\rm nloc}(\mathcal{R} \leftarrow \mathcal{R}', \tau) \\ &= \frac{\Psi_{\rm T}(\mathcal{R})}{\Psi_{\rm T}(\mathcal{R}')} \langle \mathcal{R}|{\rm e}^{-\tau \hat{W}}|\mathcal{R}'\rangle \\ &= \delta(\mathcal{R}-\mathcal{R}') - \frac{\Psi_{\rm T}(\mathcal{R})}{\Psi_{\rm T}(\mathcal{R}')} \langle \mathcal{R}|\tau \hat{W}|\mathcal{R}'\rangle + {\rm O}(\tau^2)\,, \end{aligned} \quad (25)$$

where $\hat{W}$ now combines the non-local contributions from all atoms in the system. This alone is not the desired solution, since the term involving the matrix element of $\hat{W}$ does not have a fixed sign and thus cannot be interpreted as a transition probability.

To circumvent this difficulty the so-called localization approximation has been proposed. It amounts to a replacement of the non-local operator in the hamiltonian with a local expression [93, 102, 103]

$$\hat{W} \quad \rightarrow \quad W_{\rm L}(\mathcal{R}) = \frac{\hat{W}\Psi_{\rm T}(\mathcal{R})}{\Psi_{\rm T}(\mathcal{R})}\,. \quad (26)$$

Consequently, the contributions from $\hat{W}$ are directly incorporated into the growth/decay Green's function (18) and no complications with alternating sign arise. Unfortunately, the DMC method with this approximation does not necessarily provide an upper-bound estimate for the ground-state energy. The calculated total energy $E_{\rm DMC}$ is above the lowest eigenvalue of the localized hamiltonian, which does not guarantee that it is also higher than the ground-state energy of the original hamiltonian $\hat{H}$. The errors in the total energy incurred by the localization approximation are quadratic in the difference between the trial function $|\Psi_{\rm T}\rangle$ and the exact ground-state wave function [102]. The trial wave functions are usually accurate enough for the localization error to be practically insignificant and nearly all applications listed in section 5 utilize this approximation.

A method that preserves the upper-bound property of $E_{\rm DMC}$ was proposed in the context of the DMC algorithm developed for lattice models [104]. The non-local operator $\hat{W}$ is split into two parts, $\hat{W} = \hat{W}^+ + \hat{W}^-$, such that $\hat{W}^+$ contains those matrix elements, for which $\langle \mathcal{R}|\hat{W}|\mathcal{R}'\rangle \Psi_{\rm T}(\mathcal{R})\Psi_{\rm T}(\mathcal{R}')$ is positive, and $\hat{W}^-$ contains the elements, for which the expression is negative. Only the $\hat{W}^+$ part is localized in order to obtain the approximate hamiltonian,

$$\hat{W} \quad \rightarrow \quad \hat{W}^- + \frac{\hat{W}^+\Psi_{\rm T}(\mathcal{R})}{\Psi_{\rm T}(\mathcal{R})}\,. \quad (27)$$

One can explicitly show that the lowest eigenvalue of this partially localized hamiltonian is an upper bound to the lowest eigenvalue of the original fully non-local hamiltonian [104]. Recently, a stochastic representation of the non-local Green's function (25) corresponding to $\hat{W}^-$ was implemented also into the DMC method for continuous space [105]. Apart from the recovered upper-bound property, the new algorithm reduces fluctuations of the local energy for certain types of pseudopotentials. On the other hand, the time step error is in general larger [105, 106], since the distinct treatment of the $\hat{W}^+$ and $\hat{W}^-$ parts of the pseudopotential essentially corresponds to a Trotter splitting of the growth/decay Green's function (18) into two pieces. Very recently, a more accurate Trotter break-up and other modifications improving efficiency of this method have been proposed for both continuous and lattice DMC formulations [107].

The localization approximation is directly applicable also to the fixed-phase DMC method. Adaptation of the non-local moves representing $\hat{W}^-$ to cases involving complex wave functions has not been reported yet, nevertheless, the modifications required should be only minor.

3 From a finite supercell to the thermodynamic limit

Quantum Monte Carlo methods introduced in the preceding chapter can be straightforwardly applied to physical systems of a finite size, such as atoms and clusters of atoms. To allow investigation of bulk properties of solids, the algorithms described so far have to be complemented with additional techniques that reduce the essentially infinitely many degrees of freedom into a problem of manageable proportions.

3.1 Twist-averaged boundary conditions

In approximations that model electrons in solids as an ensemble of independent (quasi-)particles, it is possible to map the whole infinite crystal onto a finite volume so that the thermodynamic limit becomes directly accessible. Hamiltonians of such models are invariant with respect to separate translations of electrons by any lattice vector $\boldsymbol{R}$, that is, for each i we can write

$$\hat{H}(\boldsymbol{r}_1, \boldsymbol{r}_2, \dots, \boldsymbol{r}_i + \boldsymbol{R}, \dots) = \hat{H}(\boldsymbol{r}_1, \boldsymbol{r}_2, \dots, \boldsymbol{r}_i, \dots)\,. \quad (28)$$

This invariance allows to diagonalize the hamiltonian only in the primitive cell of the lattice and then use the translations to expand the eigenstates from there into the whole crystal. Unfortunately, the explicit two-body interactions that we are set out to keep in the hamiltonian break the symmetry (28). The only translation left is a simultaneous displacement of all electrons by a lattice vector, which is not enough to reach the thermodynamic limit with a finite set of degrees of freedom.

To proceed further we introduce artificial translational symmetries with the aid of the so-called supercell approximation that is widely used within the independent-particle methods to investigate non-periodic structures such as lattice defects. We select a supercell having a volume Ω_S that contains several (preferably many) primitive cells. The whole crystal is then reconstructed via translations of this large cell by supercell lattice vectors $\{\boldsymbol{R}_S\}$, which are a subset of all lattice vectors $\{\boldsymbol{R}\}$. Simultaneously, we divide the electrons in the solid into groups containing $N = \rho_{\mathrm{av}}\Omega_S$ particles, where ρ_{av} is the average electron density in the crystal. This partitioning is used to construct a model hamiltonian, where electrons within each group interact, whereas there are no interactions between the groups,

$$\hat{H}_{\mathrm{model}} = \sum_{I=1}^{\infty} \hat{H}_S\big(\mathcal{R}^{(I)}\big) = \sum_{I=1}^{\infty}\left[\sum_{i=1}^{N} \hat{h}\big(\boldsymbol{r}_i^{(I)}\big) + \hat{V}_{ee}\big(\mathcal{R}^{(I)}\big)\right]. \quad (29)$$

The vector $\mathcal{R}^{(I)} = \big(\boldsymbol{r}_1^{(I)}, \dots, \boldsymbol{r}_N^{(I)}\big)$ denotes coordinates of the electrons belonging to the I-th group. Note that these electrons are not confined to any particular region in the crystal. The supercell hamiltonian $\hat{H}_S$ consists of single-particle terms $\hat{h}$, which encompass kinetic energy as well as ionic and all external potentials, and of an electron-electron contribution

$$\hat{V}_{ee}(\mathcal{R}) = \sum_{j<i} \frac{1}{|\boldsymbol{r}_i - \boldsymbol{r}_j|} + \sum_i \left[\frac{1}{2}\sum_{j,\boldsymbol{R}_S\neq 0} \frac{1}{|\boldsymbol{r}_i - \boldsymbol{r}_j - \boldsymbol{R}_S|}\right]. \quad (30)$$

The first term in (30) represents the explicit Coulomb interaction among electrons in the N-member group, and the second term mimics the interactions with the electrons outside the group. The physical meaning of the latter term is as follows: A set of images is associated with each electron j, and these virtual particles are placed at positions $\boldsymbol{r}_j + \boldsymbol{R}_S$ so that they create a regular lattice. The combination of all images has the same average charge density as the original crystal and thus represents a reasonable environment for the selected N electrons. Each electron i then interacts with the arrays of charges associated with the other electrons in the group as well as with its own images. Only one half of the interaction energy with images is included in (30), the other half belongs to the rest of the system and is distributed among the other members of the sum in (29). The model hamiltonian $\hat{H}_{\mathrm{model}}$ approaches the original fully interacting hamiltonian as N increases and a larger fraction of the interactions has the exact form.

Hamiltonians $\hat{H}_S$ and $\hat{H}_{\mathrm{model}}$ possess the symmetry described by (28) with lattice translations $\boldsymbol{R}$ replaced with $\boldsymbol{R}_S$. Consequently, the eigenfunctions of $\hat{H}_S$ are many-particle Bloch waves

$$\Psi_{\boldsymbol{K}\alpha}(\mathcal{R}) = U_{\boldsymbol{K}\alpha}(\mathcal{R}) \exp\left(\mathrm{i}\boldsymbol{K}\cdot\sum_{i=1}^{N}\boldsymbol{r}_i\right), \quad (31)$$

where α is a many-body analogue of the band index and $\boldsymbol{K}$ is the crystal momentum [108, 109]. The wave functions of the form (31) can be found in the same way as the single-particle Bloch waves within the independent-particle methods—as solutions to a problem of N particles confined to a simulation cell defined by vectors $\boldsymbol{L}_1$, $\boldsymbol{L}_2$ and $\boldsymbol{L}_3$ belonging to the set $\{\boldsymbol{R}_S\}$ and giving $\Omega_S = \big|\boldsymbol{L}_1\cdot(\boldsymbol{L}_2\times\boldsymbol{L}_3)\big|$. The dynamics of this finite N-particle system is governed by the hamiltonian $\hat{H}_S$ complemented with the so-called twisted boundary conditions [110]

$$\Psi_{\boldsymbol{K}\alpha}(\boldsymbol{r}_1, \dots, \boldsymbol{r}_i + \boldsymbol{L}_m, \dots, \boldsymbol{r}_N) = \Psi_{\boldsymbol{K}\alpha}(\boldsymbol{r}_1, \dots, \boldsymbol{r}_i, \dots, \boldsymbol{r}_N)\,\mathrm{e}^{\mathrm{i}\boldsymbol{K}\cdot\boldsymbol{L}_m}\,, \quad (32)$$

where $i = 1, \dots, N$ and $m = 1, 2, 3$. The indistinguishability of electrons implies that the phase factor is the same irrespective of which electron is moved,

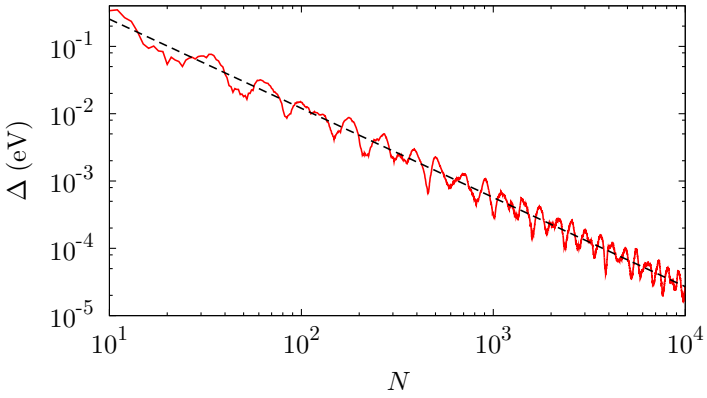

Figure 1: Deviation of the twist-averaged total energy (35) from the exact thermodynamic limit E_∞, $\Delta = [E_S(N) - E_\infty]/N$, for a three-dimensional gas of non-interacting electrons with dispersion relation $\epsilon_{\boldsymbol{k}} = k^2/2$ at density ρ corresponding to $r_\mathrm{s} = [3/(4\pi\rho)]^{1/3} = 1$. The dashed line represents the average asymptotic decay of Δ that behaves as $N^{-1.32}$.

and therefore only a single K vector common to all electron coordinates is allowed in (31) and (32). Once the quantum-mechanical problem in the finite simulation cell is solved, wave functions for the whole crystal can be constructed. Since there are no interactions between individual N-particle groups, these wave functions have the form of an antisymmetrized product of the Bloch functions (31), namely

$$\Psi_{\{\boldsymbol{K}_I\}\{\alpha_I\}}(\{\boldsymbol{r}\}) = \mathcal{A}\left[\prod_{I=1}^{\infty} \Psi_{\boldsymbol{K}_I\alpha_I}(\mathcal{R}^{(I)})\right]. \qquad (33)$$

The indicated antisymmetrization is straightforward as long as all $\boldsymbol{K}_I$ in the product are different, because each factor $\Psi_{\boldsymbol{K}_I\alpha_I}$ then comes from a disjoint part of the Fock space. The total energy corresponding to the wave function (33) with the extra restriction $\boldsymbol{K}_I \neq \boldsymbol{K}_{I'}$ reads

$$E_{\{\boldsymbol{K}_I\neq\boldsymbol{K}_{I'}\}\{\alpha_I\}} = \sum_{I=1}^{\infty} \langle \Psi_{\boldsymbol{K}_I\alpha_I} | \hat{H}_S | \Psi_{\boldsymbol{K}_I\alpha_I} \rangle \qquad (34)$$

and the lowest energy is obtained by setting $\alpha_I = 0$, that is, by selecting the ground state for each of the different boundary conditions. Although unlikely, it is possible that the true ground state of $\hat{H}_\mathrm{model}$ falls outside the constraint $\boldsymbol{K}_I \neq \boldsymbol{K}_{I'}$. In those cases, the expression (34) with $\alpha_I = 0$ is an upper-bound estimate of the actual ground-state energy of $\hat{H}_\mathrm{model}$ with a bias diminishing as N increases. Taking into account the continuous character of the momentum $\boldsymbol{K}$ in the infinite crystal and the fact that all possible boundary conditions (32) are exhausted by all K vectors within the first Brillouin zone, the ground-state energy per simulation cell can be written as

$$E_S = \langle \hat{H}_S \rangle \equiv \frac{\Omega_S}{(2\pi)^3} \int_{1.\mathrm{B.Z.}} \mathrm{d}^3K \, \langle \Psi_{\boldsymbol{K}0} | \hat{H}_S | \Psi_{\boldsymbol{K}0} \rangle . \qquad (35)$$

The total energy as well as expectation values of other periodic operators are calculated as an average over all twisted boundary conditions [110, 111]. In practice, the integral in (35) is approximated by a discrete sum. The larger the simulation cell the smaller number of K points is needed to represent the integral, since the first Brillouin zone of the simulation cell shrinks and the K-dependence of the integrand gets weaker with increasing Ω_S.

Formula (35) is *almost* identical to the expression used in supercell calculations within the independent-particle theories, the only difference is that the number of electrons at each K point is fixed to N. This constraint is benign in the case of insulators where the number of occupied bands is indeed constant across the Brillouin zone. In metals, however, the number of occupied bands fluctuates from one K point to another, and therefore the average (35) does not coincide with the exact thermodynamic limit. Figure 1 provides an illustration of the residual error. In principle, it is possible to remove this error with the aid of the grand-canonical description of the simulation cell [110], but this concept is not straightforward to apply since the supercell is no longer charge neutral.

3.2 Ewald formula

Our definition of the simulation-cell hamiltonian $\hat{H}_S$ in the preceding section was only formal and deserves a further commentary. It turns out that $\hat{V}_{ee}$ is not absolutely convergent, and therefore it does not unambiguously specify the interaction energy. In particular, the seemingly periodic form of the sums in (30) does not by itself imply the desired periodicity of the hamiltonian. However, enforcing this periodicity as an additional constraint makes the definition unique and the resulting quantity is known as the Ewald energy $\hat{V}_{ee}^{(\mathrm{E})}$. It can be shown that the requirement of periodicity is equivalent to a particular boundary condition imposed on the electrostatic potential at infinity [112, 113]. The peculiar convergence properties of the sums in (30) are a manifestation of the long-range

character of the Coulomb potential—the boundary of the sample is never irrelevant, no matter how large its volume is. Consequently, careful considerations are required in order to perform the thermodynamic limit correctly.

For the purposes of practical evaluation in QMC simulations, the Ewald energy is written as

$$\hat{V}_{ee}^{(\mathrm{E})}(\mathcal{R}) = \sum_{j<i} V_{\mathrm{E}}(\boldsymbol{r}_i - \boldsymbol{r}_j) + \frac{N}{2} \lim_{r\to 0}\left(V_{\mathrm{E}}(\boldsymbol{r}) - \frac{1}{|\boldsymbol{r}|}\right), \quad (36)$$

where $V_{\mathrm{E}}(\boldsymbol{r}_i - \boldsymbol{r}_j)$ stands for an electrostatic potential at $\boldsymbol{r}_i$ induced by the charge at $\boldsymbol{r}_j$ together with its images located at $\boldsymbol{r}_j + \boldsymbol{R}_S$. An explicit formula for the Ewald pair potential V_{E} reads [112, 114]

$$\begin{aligned} V_{\mathrm{E}}(\boldsymbol{r}_i - \boldsymbol{r}_j) &= \sum_{\boldsymbol{R}_S} \frac{1}{|\boldsymbol{r}_i - \boldsymbol{r}_j - \boldsymbol{R}_S|} \operatorname{erfc}\bigl(\kappa|\boldsymbol{r}_i - \boldsymbol{r}_j - \boldsymbol{R}_S|\bigr) \\ &\quad + \frac{4\pi}{\Omega_S} \sum_{\boldsymbol{G}_S\neq 0} \frac{1}{G_S^2} \exp\left[-\frac{G_S^2}{4\kappa^2} + \mathrm{i}\boldsymbol{G}_S\cdot(\boldsymbol{r}_i - \boldsymbol{r}_j)\right] \\ &\quad - \frac{\pi}{\Omega_S\kappa^2}\,, \end{aligned} \quad (37)$$

where $\boldsymbol{G}_S$ are vectors reciprocal to $\boldsymbol{R}_S$, $\exp(\mathrm{i}\boldsymbol{G}_S \cdot \boldsymbol{R}_S) = 1$, and κ is an arbitrary positive constant that does not alter the value of V_{E}. The omission of the $\boldsymbol{G}_S = 0$ term in the reciprocal sum corresponds to the removal of the homogeneous component from the potential V_{E}. When evaluating the total energy of a charge neutral crystal, these "background" contributions exactly cancel among the Ewald energies of electron-electron, electron-ion and ion-ion interactions.

The important feature of the Ewald formula (37) is the decomposition of the slowly converging Coulomb sum into two rapidly converging parts, one in real space and the other in reciprocal space. The break-up is not unique (not only due to the arbitrariness of κ) and can be further optimized for computational efficiency [115, 116].

3.3 Extrapolation to the thermodynamic limit

The total energy per electron $\epsilon_N = E_S/N$ evaluated according to the outlined recipe still depends on the size of the simulation cell. These residual finite-size effects can be removed by an extrapolation: Energy ϵ_N is calculated in simulation cells of several sizes and an appropriate function $\epsilon^{\mathrm{fit}}(N) = \epsilon_\infty + f(N)$ is subsequently fitted through the acquired data. In the end, ϵ_∞ is the desired energy per electron in the thermodynamic limit, where the error term $f(N)$ by definition vanishes, $\lim_{N\to\infty} f(N) = 0$. Experience with a wide range of systems [10, 117–119] indicates that as long as the integral over the Brillouin zone in (35) is well converged, the finite-size data are well approximated by a smooth function $f(N) < 0$ dominated by a $1/N$ contribution.[1] The size extrapolation is therefore quite straightforward, although often computationally expensive due to the relatively slow decay of the error term.

The origin and behaviour of the finite-size effects is a subject of ongoing investigations with the aim to find means of accelerating the convergence of the total energy and other expectation values to the thermodynamic limit. Furthermore, understanding the dependence of the finite-size errors on various parameters, such as particle density, can reduce the number of explicit size extrapolations needed to obtain quantities of interest. In calculations of equations of state (section 5.3), for instance, it is then sufficient to perform the extrapolation only at selected few, instead of all, electron densities [119].

It turns out that, in the twist-averaged expectation values $\langle\hat{H}_S\rangle$ calculated in finite simulation cells, both the hamiltonian and the wave function contain biases that contribute to the $1/N$ asymptotics of the error term $f(N)$. It was argued [113, 120] that the slow converging parts of the hamiltonian reside in the exchange-correlation energy

$$V_{\mathrm{XC}} = \langle\hat{V}_{ee}^{(\mathrm{E})}\rangle - \frac{1}{2}\int_{\Omega_S\times\Omega_S} \rho(\boldsymbol{r})V_{\mathrm{E}}(\boldsymbol{r}-\boldsymbol{r}')\rho(\boldsymbol{r}')\,\mathrm{d}^3r\mathrm{d}^3r' \quad (38)$$

defined as a difference between the expectation value of the Ewald energy $\langle\hat{V}_{ee}^{(\mathrm{E})}\rangle$ and the Hartree term that describes the interaction of the charge densities $\rho(\boldsymbol{r}) = \langle\hat{\rho}(\boldsymbol{r})\rangle$. The Hartree energy is found to converge rather rapidly with the size of the simulation cell. In systems with cubic and higher symmetry, the leading contribution to $f(N)$ can be written as [121]

$$\begin{aligned} f_{\mathrm{XC}}(N) &= \frac{V_{\mathrm{XC}}}{N} - \lim_{N\to\infty}\frac{V_{\mathrm{XC}}}{N} \\ &= -\frac{2\pi}{\Omega_S}\lim_{G_S\to 0}\frac{S(\boldsymbol{G}_S)}{G_S^2}\,. \end{aligned} \quad (39)$$

This formula involves the static structure factor

$$S(\boldsymbol{G}_S) = \frac{1}{N}\Bigl[\langle\hat{\rho}(\boldsymbol{G}_S)\hat{\rho}(-\boldsymbol{G}_S)\rangle - \bigl|\langle\hat{\rho}(\boldsymbol{G}_S)\rangle\bigr|^2\Bigr], \quad (40)$$

[1] The finite-size scaling depends on the dimensionality of the problem and the $1/N$ dependence corresponds to three-dimensional samples considered here.

where $\hat{\rho}(\boldsymbol{G}_S)$ is a Fourier component of the density operator. The exact small-momentum asymptotics of the structure factor in Coulomb systems is given by the random phase approximation (RPA) [122] and reads $S(\boldsymbol{G}_S) \sim G_S^2$, which ensures that the limit in (39) is well defined. In systems with lowered symmetry and for less accurate approximations, as is the Hartree–Fock theory where $S(\boldsymbol{G}_S) \sim G_S$, the expression for $f_{\mathrm{XC}}(N)$ must be appropriately modified [123].

The random phase approximation provides insight also into the finite-size effects induced by restricting the wave function into a finite simulation cell. According to the RPA, the many-body wave function in Coulomb systems factorizes as

$$\Psi(\mathcal{R}) = \Psi_{\mathrm{s.r.}}(\mathcal{R}) \exp\left[-\sum_{j<i} u(\boldsymbol{r}_i - \boldsymbol{r}_j)\right], \qquad (41)$$

where $\Psi_{\mathrm{s.r.}}$ contains only short-range correlations and the function $u(\boldsymbol{r})$ decays as $1/r$ at large distances. Such long-range behaviour is not consistent with the boundary conditions (32), and a truncation of this tail is therefore unavoidable. The corresponding finite-size bias is most pronounced in the expectation value of the kinetic energy $T = \langle \hat{T} \rangle$ and contributes an error term [121]

$$\begin{aligned} f_T(N) &= \frac{T}{N} - \lim_{N\to\infty} \frac{T}{N} \\ &= -\frac{1}{4\Omega_S} \lim_{G_S\to 0} G_S^2\, u(\boldsymbol{G}_S)\,, \end{aligned} \qquad (42)$$

where $u(\boldsymbol{G}_S) \sim 1/G_S^2$ is a Fourier component of $u(\boldsymbol{r})$.

Assuming that we are able to evaluate the expressions (39) and (42), we can decompose $f(N)$ into parts $f(N) = f_{\mathrm{XC}}(N) + f_T(N) + f'(N)$, where $f'(N)$ is substantially smaller than $f(N)$ and the size extrapolation is therefore better controlled. In the case of the homogeneous electron gas, the RPA provides analytic expressions for the small momentum behaviour of the required quantities $S(\boldsymbol{G}_S) \approx G_S^2/(2\omega_{\mathrm{p}})$ and $u(\boldsymbol{G}_S) \approx 4\pi/(G_S^2\omega_{\mathrm{p}})$, where $\omega_{\mathrm{p}} = \sqrt{4\pi N/\Omega_S}$ is the plasma frequency. Subsequently, the individual error terms simplify to

$$f_{\mathrm{XC}}(N) = -\frac{1}{N}\,\frac{\omega_{\mathrm{p}}}{4} \quad \text{and} \quad f_{\mathrm{T}}(N) = -\frac{1}{N}\,\frac{\omega_{\mathrm{p}}}{4}\,. \quad (43)$$

It can be demonstrated that these two contributions completely recover the $1/N$ part of $f(N)$, and that the residual term $f'(N)$ scales as $\sim N^{-4/3}$ [123].

Application of the derived finite-size corrections to simulations of realistic solids is less straightforward since reliable analytic results are not available. The small momentum asymptotics of $S(\boldsymbol{G}_S)$ and $u(\boldsymbol{G}_S)$ have to be examined numerically. Sufficiently large simulation cells are needed for this purpose, since the smallest nonzero reciprocal vector available in a supercell with volume Ω_S is $G_S \sim \Omega_S^{-1/3}$. Utilization of the kinetic energy correction (42) within DMC simulations is further complicated by the fact that the function $u(\boldsymbol{r})$ is not given as an expectation value of an operator, and thus it is not clear how it could be extracted from the sampled mixed distribution $\Psi_{\mathrm{D}}^*\Psi_{\mathrm{T}}$. One has to rely on the trial wave function alone to correctly reproduce the long-range tail (41), which can be a challenging task in simulation cells containing a large number of electrons.

The above analysis employs exact analytic formulae or quantum Monte Carlo simulations themselves to find corrections to the finite-size biases. Alternatively, it is possible to adopt a more heuristic approach and estimate the finite-size effects within an approximative method. For instance, the error term $f(N)$ can be rewritten as $f(N) = \epsilon_S^{(\mathrm{LDA})} - \epsilon_\infty^{(\mathrm{LDA})} + f''(N)$, where $\epsilon_S^{(\mathrm{LDA})}$ and $\epsilon_\infty^{(\mathrm{LDA})}$ are total energies per particle provided by the local density approximation with two distinct exchange-correlation functionals, and $f''(N)$ is anticipated to be considerably smaller than $f(N)$ [124]. The exchange-correlation functional corresponding to $\epsilon_\infty^{(\mathrm{LDA})}$ is constructed from properties of the homogeneous electron gas in the thermodynamic limit (in other words, it is the standard LDA functional), the functional leading to $\epsilon_S^{(\mathrm{LDA})}$ is based on the homogeneous electron gas confined to the same finite supercell as the quantum system under investigation. The latter functional is not universal and needs to be found for each simulation cell separately at the cost of auxiliary simulations of the homogeneous Coulomb gas.

3.4 An alternative model for Coulomb interaction energy

The expression for the electron-electron interaction energy $\hat{V}_{ee}^{(\mathrm{E})}$ has two properties: (i) it is periodic and (ii) corresponds to an actual, albeit artificial, system of point charges. Although the latter property is conceptually convenient, it is not really necessary, and any periodic potential that exhibits the correct behaviour in the limit of the infinitely large simulation cell is legitimate. Relaxation of the constraint (ii) in favour of faster convergence of the total energy per particle ϵ_N to its thermodynamic limit was explored in a series of papers [113, 120, 125], where the so-called model periodic Coulomb (MPC) interaction was proposed.

The replacement for the Ewald energy $\hat{V}_{ee}^{(\mathrm{E})}$ reads

$$\hat{V}_{ee}^{(\mathrm{MPC})}(\mathcal{R}) = \sum_{j<i} \frac{1}{|\boldsymbol{r}_i - \boldsymbol{r}_j|_\mathrm{m}} + \sum_i \int_{\Omega_S} \left[V_\mathrm{E}(\boldsymbol{r}_i - \boldsymbol{r}) - \frac{1}{|\boldsymbol{r}_i - \boldsymbol{r}|_\mathrm{m}} \right] \rho(\boldsymbol{r}) \, \mathrm{d}^3 r - \int_{\Omega_S \times \Omega_S} \left[V_\mathrm{E}(\boldsymbol{r} - \boldsymbol{r}') - \frac{1}{|\boldsymbol{r} - \boldsymbol{r}'|_\mathrm{m}} \right] \rho(\boldsymbol{r}) \rho(\boldsymbol{r}') \, \mathrm{d}^3 r \mathrm{d}^3 r' \,, \quad (44)$$

where $|\boldsymbol{r} - \boldsymbol{r}'|_\mathrm{m} = \min_{\boldsymbol{R}_S} |\boldsymbol{r} - \boldsymbol{r}' + \boldsymbol{R}_S|$ stands for the so-called minimum image distance. The operator $\hat{V}_{ee}^{(\mathrm{MPC})}$ is constructed in such a way that the Hartree part of its expectation value is the same as in the Ewald method, whereas the slowly converging contribution to the exchange-correlation energy is removed. Therefore, the MPC interaction is essentially equivalent to the Ewald formula (36) complemented with the *a posteriori* correction (39). Instead of the structure factor, it is the one-particle density ρ that has to be evaluated as an extra quantity in this case (unless it is known exactly as in a homogeneous system). The explicit presence of the density ρ in the hamiltonian is inconvenient for the DMC method where the local energy is needed from the start of the simulation, that is, before the density data could be accumulated. The situation can be remedied by replacing the unknown density ρ with an approximation ρ_A. For instance, the one-particle density provided by DFT is usually quite accurate. The error introduced by this substitution is proportional to $(\rho - \rho_A)^2$ and further diminishes as the simulation cell increases. The Ewald and MPC energies per particle are therefore the same in the thermodynamic limit even if the approximate charge density is used [123, 126].

4 Trial wave functions

Accurate trial wave functions are essential for successful applications of the quantum Monte Carlo methods. The quality of the employed wave functions influences the statistical efficiency of the simulations as well as the accuracy of the achieved results. Equally important, especially for investigations of extended systems, is the possibility to quickly compute the wave function value and its derivatives ($\nabla\Psi_\mathrm{T}$ and $\nabla^2\Psi_\mathrm{T}$), since these quantities usually represent the most computationally costly part of the whole simulation. Compact expressions are therefore strongly preferred.

A significant part of the construction of the trial wave functions is optimization of the variational parameters introduced into the functional form representing Ψ_T. It is a non-trivial task since the number of parameters is often large, Ψ_T depends non-linearly on them, and the quantity to be minimized (E_VMC or the variance of the local energy) is a fluctuating number. Several powerful methods addressing these problems have been developed during the years [127–130] and even hundreds of parameters can be optimized with good efficiency nowadays.

4.1 Elementary properties

Since our aim is the electronic structure, and the electrons are subject to the Pauli exclusion principle, our trial wave functions have to be antisymmetric with respect to pair-electron exchanges. We assume collinear spins that are independent of electron positions, and therefore the full wave function $\widetilde{\Psi}_\mathrm{T}$ can be factorized as

$$\widetilde{\Psi}_\mathrm{T}(\mathcal{R}, \mathcal{S}) = \sqrt{\frac{N_\uparrow! \, N_\downarrow!}{N!}} \sum_C (-1)^C \times \Psi_\mathrm{T}(C\mathcal{R}) \left| C\{\underbrace{\uparrow \ldots \uparrow}_{N_\uparrow} \underbrace{\downarrow \ldots \downarrow}_{N_\downarrow}\} \right\rangle , \quad (45)$$

where $\mathcal{S} = (\sigma_1, \ldots, \sigma_N)$ is a vector consisting of $N = N_\uparrow + N_\downarrow$ spin variables. The sum runs over all distinct states of $N_\uparrow$ up-oriented and $N_\downarrow$ down-oriented spins. In the case of $N_\uparrow = 2$ and $N_\downarrow = 1$ the spin states are $|\uparrow_1\uparrow_2\downarrow_3\rangle$, $|\uparrow_1\uparrow_3\downarrow_2\rangle$ and $|\uparrow_2\uparrow_3\downarrow_1\rangle$, and the corresponding $C\mathcal{R}$ combinations are $\{\boldsymbol{r}_1, \boldsymbol{r}_2, \boldsymbol{r}_3\}$, $\{\boldsymbol{r}_1, \boldsymbol{r}_3, \boldsymbol{r}_2\}$ and $\{\boldsymbol{r}_2, \boldsymbol{r}_3, \boldsymbol{r}_1\}$. The spatial-only part Ψ_T is antisymmetric with respect to exchanges of parallel electrons and its symmetry with respect to exchanges of antiparallel electrons is unrestricted. The sum in (45) with the appropriate sign factors $(-1)^C$ represents the residual antisymmetrization for the antiparallel spins.

Both $\widetilde{\Psi}_\mathrm{T}$ and Ψ_T are normalized to unity and identity $\langle\widetilde{\Psi}_\mathrm{T}|\hat{A}|\widetilde{\Psi}_\mathrm{T}\rangle = \langle\Psi_\mathrm{T}|\hat{A}|\Psi_\mathrm{T}\rangle$ holds for any spin-independent operator $\hat{A}$ since the spin states $\left|C\{\uparrow \ldots \uparrow\downarrow \ldots \downarrow\}\right\rangle$ are mutually orthonormal. Therefore, it is usually sufficient to consider only the spatial part Ψ_T of the full many-body wave function in applications of the VMC and DMC methods, and we limit our discussion to Ψ_T from now on.[2]

Our goal is for the local energy $\hat{H}\Psi_\mathrm{T}/\Psi_\mathrm{T}$ to be very close to a hamiltonian eigenvalue and fluctuating as little as possible. In systems with charged particles interacting via the Coulomb potentials, it requires that the kinetic energy proportional to $\nabla^2\Psi_\mathrm{T}$ contains

[2] In fact, the DMC algorithm is defined only for the spatial part Ψ_T, consult sections 2.2.2 and 2.2.4. Decomposition (45) then provides a hint how to calculate expectation values of spin-dependent operators from the sampled mixed distribution $\Psi_\mathrm{D}^*\Psi_\mathrm{T}$.

singularities which cancel the $1/r$ divergencies of the potential. This cancellation is vital for controlling the statistical uncertainties of the Monte Carlo estimate of the total energy and takes place when Kato cusp conditions are fulfilled [131, 132].

At electron-electron coincidences, these conditions can be formulated with the aid of projections of the trial wave function Ψ_T onto spherical harmonics Y_{lm} centered at the coincidence point,

$$\Psi_\mathrm{T}^{(l,m)}(r_{ij}, \boldsymbol{r}_\mathrm{c.m.}, \mathcal{R} \setminus \{\boldsymbol{r}_i, \boldsymbol{r}_j\}) = \frac{1}{r_{ij}^l} \int_{4\pi} \Psi_\mathrm{T}(\mathcal{R}) Y_{lm}^*(\Omega_{ij}) \mathrm{d}\Omega_{ij} \,. \quad (46)$$

In this definition, the following notation has been introduced: $r_{ij} = |\boldsymbol{r}_{ij}| = |\boldsymbol{r}_i - \boldsymbol{r}_j|$ is the electron-electron distance, Ω_{ij} is the spherical angle characterizing orientation of the vector $\boldsymbol{r}_{ij}$, and $\boldsymbol{r}_\mathrm{c.m.} = (\boldsymbol{r}_i + \boldsymbol{r}_j)/2$ is the position of the center of mass of the electron pair. The cusp conditions can then be written as

$$\lim_{r_{ij}\to 0} \frac{1}{\Psi_\mathrm{T}^{(0,0)}} \frac{\partial \Psi_\mathrm{T}^{(0,0)}}{\partial r_{ij}} = \frac{1}{2} \quad (47)$$

for unlike spins and

$$\lim_{r_{ij}\to 0} \frac{1}{\Psi_\mathrm{T}^{(1,m)}} \frac{\partial \Psi_\mathrm{T}^{(1,m)}}{\partial r_{ij}} = \frac{1}{4} \quad (48)$$

for like spins. The expressions (47) and (48) differ because Ψ_T is an odd function with respect to $\boldsymbol{r}_{ij}$ in the latter case, which implies $\Psi_\mathrm{T}^{(0,0)} = 0$.

Analogous cusps occur in all-electron calculations when electrons approach nuclei. Unless the s-wave component $\Psi_\mathrm{T}^{(0,0)}$ vanishes (for a general discussion see [132]), it can be shown that

$$\lim_{r_{Ii}\to 0} \frac{1}{\Psi_\mathrm{T}^{(0,0)}} \frac{\partial \Psi_\mathrm{T}^{(0,0)}}{\partial r_{iI}} = -Z_I \,, \quad (49)$$

where r_{iI} is the electron-nucleus distance and Z_I is the charge of the nucleus.

A convenient functional form that meets the specified criteria is a product of an antisymmetric part Ψ_A and a positive symmetric expression $\exp(-U_\mathrm{corr})$ [133],

$$\Psi_\mathrm{T}(\mathcal{R}) = \Psi_\mathrm{A}(\mathcal{R}) \, \exp\bigl[-U_\mathrm{corr}(\mathcal{R})\bigr] \,. \quad (50)$$

The Jastrow correlation factor $\exp(-U_\mathrm{corr})$ incorporates the electron-electron cusp conditions (47) and (48), and Ψ_A ensures the fermionic character of the wave function. The electron-ion cusps (49) can be included in either Ψ_A [63, 94, 134, 135] or in the correlation factor [136]. In simulations of extended systems, the antisymmetric part obeys the twisted boundary conditions (section 3.1) and $\exp(-U_\mathrm{corr})$ is periodic at the boundaries of the simulation cell. We discuss the individual parts of the trial wave function (50) in some detail next.

4.2 Jastrow factor

The majority of applications fits into a framework set by the expression

$$U_\mathrm{corr}(\mathcal{R}) = \sum_i \chi_{\sigma_i}(\boldsymbol{r}_i) + \sum_{j<i} u_{\sigma_i\sigma_j}(\boldsymbol{r}_i, \boldsymbol{r}_j) \,, \quad (51)$$

where the functions χ and u take a specific parametrized form [61, 137, 138] and can depend also on spins of the involved electrons as indicated by the indices $\sigma \in \{\uparrow, \downarrow\}$. The inclusion of the uncorrelated one-body terms χ is important especially if the trial wave function is optimized with a fixed antisymmetric part Ψ_A [51, 101, 139]. The two-body terms u are typically simplified to

$$\sum_{j<i} u_{\sigma_i\sigma_j}(\boldsymbol{r}_i, \boldsymbol{r}_j) \to \sum_{j<i} u_\mathrm{ee}(\boldsymbol{r}_{ij}) + \sum_{j<i,I} u_\mathrm{een}(|\boldsymbol{r}_{ij}|, |\boldsymbol{r}_{iI}|, |\boldsymbol{r}_{jI}|) \,, \quad (52)$$

where u_ee is an expression corresponding to a homogeneous system and the electron-electron-nucleus term u_een takes into account the differences between the two-body correlations in high-density regions near nuclei and in low density regions far from them. Spin indices were dropped to simplify the notation. The u_een contribution can usually be short ranged in the $|\boldsymbol{r}_{ij}|$ parameter, whereas the simpler u_ee term is preferably long ranged in order to approximate the RPA asymptotics (41) as closely as allowed by the given simulation cell [10, 136]. Of course, limited computational resources can (and often do) enforce further simplifying compromises. In simulations of homogeneous fermion fluids (electron gas, ^{3}He), on the other hand, even higher order correlations were successfully included: three-particle [9, 140–143] as well as four-particle [144].

4.3 Slater–Jastrow wave function

The simplest antisymmetric form that can be used in place of Ψ_A in (50) is a product of two Slater determinants,

$$\Psi_\mathrm{A}^\mathrm{Slater}(\mathcal{R}) = \mathcal{A}\bigl[\psi_1^\uparrow(\boldsymbol{r}_1^\uparrow) \dots \psi_{N_\uparrow}^\uparrow(\boldsymbol{r}_{N_\uparrow}^\uparrow)\bigr] \times \mathcal{A}\bigl[\psi_1^\downarrow(\boldsymbol{r}_1^\downarrow) \dots \psi_{N_\downarrow}^\downarrow(\boldsymbol{r}_{N_\downarrow}^\downarrow)\bigr] = \det\bigl[\psi_n^\uparrow(\boldsymbol{r}_i^\uparrow)\bigr] \det\bigl[\psi_m^\downarrow(\boldsymbol{r}_j^\downarrow)\bigr] \,, \quad (53)$$

where $\psi_n^{\uparrow}$ and $\psi_m^{\downarrow}$ are single-particle orbitals that correspond to spin-up respectively spin-down electronic states and $\psi_n^{\sigma}(\boldsymbol{r}_i^{\sigma})$ in the arguments of the determinants stands for a $N_\sigma \times N_\sigma$ matrix A_{ni}^{σ}. In quantum-chemical applications, a common strategy to improve upon the Slater wave function is to use a linear combination of several determinants,

$$\Psi_{\mathrm{A}}^{\text{m-det}}(\mathcal{R}) = \sum_{\alpha} c_\alpha \det\bigl[\psi_{\alpha,n}^{\uparrow}(\boldsymbol{r}_i^{\uparrow})\bigr] \det\bigl[\psi_{\alpha,m}^{\downarrow}(\boldsymbol{r}_j^{\downarrow})\bigr] \,. \tag{54}$$

These multi-determinantal expansions are mostly impractical for simulations of solids, since the number of determinants required to describe the wave function to some fixed accuracy increases exponentially with the system size. One case where multiple determinants are vital even in extended systems are fixed-node DMC calculations of excitation energies, since adherence to proper symmetries is essential for validity of the corresponding variational theorem [62, 145] and the trial wave functions displaying the correct symmetry are not always representable by a single determinant. In these instances, however, the expansions (54) are short.

In simulation cells subject to the twisted boundary conditions (32) specified by a supercell crystal momentum $\boldsymbol{K}$, the one-particle orbitals ψ_m^{σ} are Bloch waves satisfying

$$\psi_{\boldsymbol{K}m}^{\sigma}(\boldsymbol{r}+\boldsymbol{L}_\alpha) = \psi_{\boldsymbol{K}m}^{\sigma}(\boldsymbol{r})\, \mathrm{e}^{\mathrm{i}\boldsymbol{K}\cdot\boldsymbol{L}_\alpha} \,, \tag{55}$$

where $\alpha = 1, 2, 3$ and m is a band index in the supercell. Since the simulation cell contains several primitive cells, the crystal has a higher translational symmetry than implied by (55) and the orbitals can be conveniently re-labeled using $m \to (\boldsymbol{k}, m')$, where $\boldsymbol{k}$ and m' are a momentum and a band index defined with respect to the primitive cell. The Bloch waves fulfill also

$$\psi_{\boldsymbol{K}\boldsymbol{k}m'}^{\sigma}(\boldsymbol{r}+\boldsymbol{l}_\alpha) = \psi_{\boldsymbol{K}\boldsymbol{k}m'}^{\sigma}(\boldsymbol{r})\, \mathrm{e}^{\mathrm{i}\boldsymbol{k}\cdot\boldsymbol{l}_\alpha} \,, \tag{56}$$

where $\boldsymbol{l}_\alpha$ are lattice vectors defining the primitive cell. Assuming that the supercell is built as $\boldsymbol{L}_\alpha = n_\alpha \boldsymbol{l}_\alpha$ with integers n_α, the momenta $\boldsymbol{k}$ compatible with (55) fall onto a regular mesh

$$\boldsymbol{k} = \boldsymbol{K} + 2\pi\biggl(\frac{j_1}{n_1}\frac{\boldsymbol{l}_2\times\boldsymbol{l}_3}{\boldsymbol{l}_1\cdot(\boldsymbol{l}_2\times\boldsymbol{l}_3)} + \frac{j_2}{n_2}\frac{\boldsymbol{l}_3\times\boldsymbol{l}_1}{\boldsymbol{l}_2\cdot(\boldsymbol{l}_3\times\boldsymbol{l}_1)} + \frac{j_3}{n_3}\frac{\boldsymbol{l}_1\times\boldsymbol{l}_2}{\boldsymbol{l}_3\cdot(\boldsymbol{l}_1\times\boldsymbol{l}_2)}\biggr) \tag{57}$$

with indices j_α running from 0 to $n_\alpha - 1$. This set of k points corresponds to the Monkhorst–Pack grid [146] shifted by a vector $\boldsymbol{K}$.

A number of strategies have been devised to determine the optimal one-particle orbitals for use in the Slater–Jastrow wave functions, which certainly differ from the Hartree–Fock orbitals that minimize the variational energy only when $U_{\mathrm{corr}} = 0$. Ideally, the orbitals are parametrized by an expansion in a saturated basis with the expansion coefficients varied to minimize the VMC or DMC total energy. The stochastic noise and the computational demands of the DMC method make the minimization of E_{DMC} extremely inefficient in practice. The VMC optimization of the orbitals was successfully performed in atoms and small molecules of the first-row atoms [130, 147, 148], but the method is still too demanding for applications to solids.

To avoid the large number of variational parameters needed to describe the single-particle orbitals, another family of methods has been proposed. The orbitals in the Slater–Jastrow wave function are found as solutions to self-consistent-field equations that represent a generalization of the Hartree–Fock theory to the presence of the Jastrow correlation factor [139, 149–151]. These methods were tested in atoms as well as in solids within the VMC framework [149, 152]. Unfortunately, the wave functions derived in this way did not lead to lower DMC energies compared to wave functions with orbitals from the Hartree–Fock theory or from the local density approximation [149, 153]. It is unclear, whether the lack of observed improvements in the fermionic nodal surfaces stems from insufficient flexibility of the employed correlation factors or from the fact that only applications to weakly correlated systems were considered so far.

An even simpler approach is to introduce a parametric dependence into the self-consistent-field equations without a direct relation to the actual Jastrow factor. An example are the Kohn–Sham equations corresponding to some exchange-correlation functional, in which it is possible to identify a parameter (or several parameters) measuring the degree of correlations in the system and thus mimicking, to a certain degree, the effect of the Jastrow factor. Particular hybrid functionals with variable admixture of the exact-exchange component [37] were successfully employed for this purpose in conjunction with the DMC optimization, so that the variations of the fermionic nodal structure could be directly quantified [154–157]. Sizeable improvements of the DMC total energy associated with the replacement of the Hartree–Fock (or LDA) orbitals with the orbitals provided by the optimal hybrid functional were observed in compounds containing $3d$ elements.

Evaluation of the Slater determinants dominates the computational demands of large-scale Monte Carlo calculations, and it is therefore very important to con-

sider its implementation carefully. Notably, schemes combining a localized basis set (atom-centered Gaussians or splines [158, 159]) with a transformation of the single-particle orbitals into localized Wannier-like functions can achieve nearly linear scaling of the computational effort with the system size when applied to insulators [160–162].

4.4 Antisymmetric forms with pair correlations

Apart from the Pauli exclusion principle, the Slater determinant does not incorporate any correlations among the electrons, since it is just an antisymmetrized form of a completely factorized function, that is, of a product of one-body orbitals. A better account for correlations can be achieved by wave functions built as the appropriate antisymmetrization of a product of two-body orbitals. The resulting antisymmetric forms are called pfaffians and can generally be written as [59, 163]

$$\Psi_{\mathrm{A}}^{\mathrm{Pfaff}}(\mathcal{R}) = \mathcal{A}\Bigg[\prod_{m=1}^{N_{\mathrm{P}}} \phi_m^{\sigma_{m,1}\sigma_{m,2}}\big(\boldsymbol{r}_{m,1}^{\sigma_{m,1}}, \boldsymbol{r}_{m,2}^{\sigma_{m,2}}\big) \times \prod_{n=1}^{N-2N_{\mathrm{P}}} \psi_n^{\sigma_n}\big(\boldsymbol{r}_n^{\sigma_n}\big)\Bigg], \quad (58)$$

where N_{P} is the number of correlated pairs, $N_{\mathrm{P}} \leq N/2$. The two-body orbitals $\phi_m^{\uparrow\downarrow}$ that couple unlike-spin electrons (singlet pairs) are symmetric, whereas $\phi_m^{\uparrow\uparrow}$ and $\phi_m^{\downarrow\downarrow}$ (triplet pairs) are antisymmetric functions. The inclusion of the one-body orbitals ψ_n^{σ} allows for odd N or for only partially paired electrons. The pfaffian wave functions can be viewed as compacted forms of particular multi-determinantal expansions (54).

An important representative of the functional form (58) is the Bardeen–Cooper–Schrieffer (BCS) wave function [164] projected onto a fixed number of particles, which is obtained from (58) by considering a singlet pairing in an unpolarized system ($N_\uparrow = N_\downarrow = N/2$) with all two-body orbitals identical. In that case, the antisymmetrization reduces to a determinant [165]

$$\Psi_{\mathrm{A}}^{\mathrm{BCS}}(\mathcal{R}) = \det\big[\phi^{\uparrow\downarrow}(\boldsymbol{r}_i^{\uparrow}, \boldsymbol{r}_j^{\downarrow})\big], \quad (59)$$

where $\phi^{\uparrow\downarrow}(\boldsymbol{r}_i^{\uparrow}, \boldsymbol{r}_j^{\downarrow})$ is to be understood as a $N/2 \times N/2$ matrix A_{ij}. In the quantum-chemical literature, this functional form is also known as the antisymmetrized geminal power. Note that the form of the BCS wave function does not by itself imply formation of Cooper pairs and their condensation, since the determinant in (59) reduces to the Slater wave function (53) when the pair orbital is taken in the form

$$\phi_{\mathrm{Slater}}^{\uparrow\downarrow}(\boldsymbol{r}_i^{\uparrow}, \boldsymbol{r}_j^{\downarrow}) = \sum_{n=1}^{N/2} \psi_n^{\uparrow}(\boldsymbol{r}_i^{\uparrow})\psi_n^{\downarrow}(\boldsymbol{r}_j^{\downarrow}). \quad (60)$$

The BCS–Jastrow wave functions were employed in investigations of ultra cold atomic gases (section 5.8) [166, 167] as well as in calculations of the electronic structure of atoms [168] and molecules [169].

Trial wave functions with triplet pairing among particles were suggested in the context of liquid ^{3}He already two decades ago [165, 170]. It was realized only recently that even in these cases the exponentially large number of terms constituting the pfaffian can be rearranged in a way that facilitates its evaluation in a polynomial time, and therefore allows application of the pfaffian–Jastrow trial wave functions in conjunction with the VMC and DMC methods [163, 171].

4.5 Backflow coordinates

Another way to further increase the variational freedom of the antisymmetric part of the trial wave function is the backflow transformation $\Psi_{\mathrm{A}}(\mathcal{R}) \to \Psi_{\mathrm{A}}(\mathcal{X})$, where the new collective coordinates $\mathcal{X}$ are functions of the original electron positions $\mathcal{R}$. The designation "backflow" originates from an intuitive picture of the correlated motion of particles introduced by Feynman to describe excitations in quantum fluids [172, 173].

In order to illustrate what is the origin of such coordinates, let us consider homogeneous interacting fermions in a periodic box with a trial wave function of the Slater–Jastrow type, $\Psi_{\mathrm{T}}(\mathcal{R}) = \det\big[\exp(\mathrm{i}\boldsymbol{k}\cdot\boldsymbol{r}_i)\big] \exp\big[\sum_{i<j}\gamma(r_{ij})\big]$. The Jastrow factor is optimized so that its laplacian cancels out the interactions as much as possible within the variational freedom. Applying the kinetic energy operator to the Slater–Jastrow product results in local energy of the form

$$\frac{[\hat{H}\Psi_{\mathrm{T}}](\mathcal{R})}{\Psi_{\mathrm{T}}(\mathcal{R})} = E_{\mathrm{var}}(\mathcal{R}) - \Big(\nabla \ln\big|\det\big[\exp(\mathrm{i}\boldsymbol{k}\cdot\boldsymbol{r}_i)\big]\big|\Big)\cdot\Big(\nabla\sum_{i<j}\gamma(r_{ij})\Big), \quad (61)$$

where we can qualitatively characterize $E_{\mathrm{var}}(\mathcal{R})$ as a mildly varying function close to a constant while the second term represents a non-constant "spurious" contribution, which appears as a scalar product of two fluxes. Consider now the following modification of the Slater–Jastrow form, $\Psi_{\mathrm{T}}(\mathcal{R}) = \det\big[\exp(\mathrm{i}\boldsymbol{k}\cdot\boldsymbol{x}_i)\big] \exp\big[\sum_{i<j}\gamma(r_{ij})\big]$,

where the single-particle coordinates are modified as $\boldsymbol{x}_i = \boldsymbol{r}_i + \sum_j \boldsymbol{\vartheta}(r_{ij})$ with $\boldsymbol{\vartheta}(0) = \boldsymbol{0}$. One can show that with a proper choice of the function $\boldsymbol{\vartheta}(r_{ij})$, the laplacian of $\det\big[\exp(\mathrm{i}\boldsymbol{k}\cdot\boldsymbol{x}_i)\big]$ produces terms that cancel out most of the spurious contributions in the local energy given by (61). Of course, the backflow form generates also new non-constant terms so that the wave function has to be optimized for the overall maximum gain using variational strategies.

In general, the new coordinates are written as $\boldsymbol{x}_i = \boldsymbol{r}_i + \boldsymbol{\xi}_i(\mathcal{R})$ with $\boldsymbol{\xi}$ taken in a form analogous to the parametrization of the Jastrow factor U_{corr} (51) and (52). The vector $\boldsymbol{\xi}$ contains two-particle and possibly higher order correlations and, in systems with external potentials, also inhomogeneous one-body terms. The backflow transformation has been very successful in simulations and understanding of homogeneous quantum liquids [9, 141, 143, 144], and some progress has recently been reported in applying these techniques also to atoms and molecules [163, 174].

5 Applications

In the last part of the article we go through selected applications of the quantum Monte Carlo methodology to the electronic structure of solids. In practically all listed cases, with the exception of sections 5.1 and 5.8 dealing with model calculations, the Slater–Jastrow functional form is employed as the trial wave function. The reviewed results therefore map out the accuracy that is achievable in the realistic solids when the mean-field topology of the fermionic nodes is assumed. It is shown that the quality of the DMC predictions is remarkable despite this relatively simple approximation.

5.1 Properties of the homogeneous electron gas

The homogeneous electron gas, also referred to as jellium, is one of the simplest many-body models that can describe certain properties of real solids, especially the alkali metals. At zero temperature, the model is characterized by the densities of spin-up and spin-down electrons, $\rho_\uparrow$ and $\rho_\downarrow$, or, alternatively, by the total density $\rho = \rho_\uparrow + \rho_\downarrow$ and the spin polarization $\zeta = |\rho_\uparrow - \rho_\downarrow|/\rho$. It is convenient to express the density ρ and other quantities in terms of a dimensionless parameter $r_{\mathrm{s}} = [3/(4\pi\rho)]^{1/3}/a_{\mathrm{B}}$, where a_{B} is the Bohr radius. For example, the density of valence electrons in the sodium metal corresponds to $r_{\mathrm{s}} \approx 4$.

The total energy of jellium is particularly simple since it includes only the kinetic energy of the electrons, the Coulomb electron-electron repulsion, and a constant which represents the interaction of the electrons with an inert uniformly distributed positive charge that maintains overall charge neutrality of the system. A straightforward dimensional analysis shows that the kinetic energy dominates the Coulomb interaction at high densities (small r_{s}), where the electrons behave like a nearly ideal gas and the unpolarized state ($\zeta = 0$) is the most stable. In the limit of very low densities, on the other hand, the kinetic energy becomes negligible and the electrons "freeze" into a Wigner crystal [189].

The homogeneous electron gas at zero temperature was one of the first applications of the variational and diffusion Monte Carlo methods. In the early investigations [10, 11], only the unpolarized ($\zeta = 0$) and fully polarized ($\zeta = 1$) fluid phases were considered together with the Wigner crystal. Later, fluids with partial spin polarization were taken into account as well [190–193]. The most accurate trial wave functions (the Slater–Jastrow form with backflow correlations) were used in reference [193] where it was found that the unpolarized fluid is stable below $r_{\mathrm{s}} = 50 \pm 2$. At this density the gas undergoes a second-order phase transition into a partially polarized state, and the spin polarization ζ then monotonically increases as the fluid is further diluted. Eventually, the Wigner crystallization density is reached, for which two DMC estimates exist: $r_{\mathrm{s}} = 100 \pm 20$ [11] and $r_{\mathrm{s}} = 65 \pm 10$ [192]. The discrepancy is presumably caused by the very small energy differences between the competing phases over a wide range of densities, and by uncertainties in the extrapolation to the thermodynamic limit. Advanced finite-size extrapolation methods, outlined in section 3 earlier, could possibly shed some new light on these quantitative differences. Indeed, recent calculations show further improvements in accuracy of the total and correlation energies [194]. A number of static properties of the liquid phases that provide a valuable insight into the details of the electron correlations in the jellium model and in Coulomb systems in general were evaluated by QMC methods as well [86, 191, 193, 195].

The impact of the QMC calculations of the homogeneous electron gas [11] has been very significant because of the prominent position of the model as one of the simplest periodic many-body systems, and also due to the fact that the QMC correlation energy has become widely used as an input in density-functional calculations [35, 196].

The results quoted so far referred to the homogeneous Coulomb gas in three dimensions. The two-dimensional gas, which is realized by confining electrons to a surface, interface or to a thin layer in a semiconductor heterostructure, has received similar if not even greater attention of QMC practitioners

Table 1: Cohesive energies of solids (in eV). Shown are DMC numbers unless only VMC data are available for the particular compound; those instances are marked with (∗). The latest results are preferred in cases where multiple calculations exist. If not indicated otherwise, the experimental cohesive energies are deduced from the room-temperature formation enthalpies quoted in [188].

compound	QMC		experiment	
Li	1.09 ± 0.05	[175]	1.65	
	1.57 ± 0.01	[176] (∗)		
Na	1.14 ± 0.01	[124]	1.11	
	1.0221 ± 0.0003	[126]		
Mg	1.51 ± 0.01	[106]	1.52	
Al	3.23 ± 0.08	[177] (∗)	3.43	[177]
MgH_2	6.84 ± 0.01	[106]	6.83	
BN	12.85 ± 0.09	[178] (∗)	12.9	[179]
C (diamond)	7.346 ± 0.006	[180]	7.37	[181]
Si	4.62 ± 0.01	[182]	4.62	[183]
Ge	3.85 ± 0.10	[109]	3.86	
GaAs	4.9 ± 0.2	[184] (∗)	6.7	[185]
MnO	9.29 ± 0.04	[157]	9.5	
FeO	9.66 ± 0.04	[119]	9.7	
NiO	9.442 ± 0.002	[186]	9.5	
$BaTiO_3$	31.2 ± 0.3	[187]	31.57	

[10, 197–202]. The Wigner crystallization was predicted to occur at $r_s = 37 \pm 5$ [197],[3] a value that coincides with the density $r_s = 35 \pm 1$ where a metal–insulator transition was experimentally observed later [203].

5.2 Cohesive energies of solids

The cohesive energy measures the strength of the chemical bonds holding the crystal together. It is defined as the difference between the energy of a dilute gas of the constituent atoms or molecules and the energy of the solid. Calculation of the cohesive energy is a stringent test of the theory, since it has to accurately describe two different systems with very dissimilar electronic structure.

The first real solids whose cohesive energies were evaluated by a QMC method were carbon and silicon in the diamond crystal structure [101, 204]. These early VMC estimates were later refined with the DMC method [180, 182, 205, 206]. The most accurate results to date are shown in table 1, where we have compiled the cohesive energies of a number of compounds investigated with the quantum Monte Carlo methods. Corresponding experimental data are shown for comparison. The electronic total energy calculated in QMC simulations is not the only contribution to the cohesive energy of a crystal, and the zero-point and thermal motion of the nuclei has to be accounted for as well, especially in compounds containing light atoms. We refer the reader to the original references for details of these corrections. At present, a direct QMC determination of the phonon spectrum is generally not practicable due to unresolved issues with reliable and efficient calculation of forces acting on the nuclei [48]. The effects due to the nuclear motion are thus typically estimated within the density-functional theory.

Overall, the agreement of the DMC results with experiments is excellent; the errors are smaller than 0.1 eV most of the time, including the Na and Mg elemental metals where coping with the finite-size effects is more difficult. Notably, the diffusion Monte Carlo performs (almost) equally well in strongly correlated solids represented in table 1 by $3d$ transition metal oxides MnO, FeO and NiO. The GaAs result is an obvious outlier with a systematic error of almost 2 eV that the authors identify with the deficiencies of their pseudopotentials [184]. The two decades old application of the DMC method to the Li metal [175] is the only all-electron simulation in the list and its comparison to a subsequent pseudopotential calculation [176] suggests that a large part of the discrepancy with the experiment is due to the fixed-node errors in the high-density core regions. It is likely that a substantial improvement would be observed if the all-electron calculations were revisited with today's state of the art trial wave functions.

[3] Note that in two dimensions the dimensionless density parameter r_s is defined as $r_s = 1/(a_B\sqrt{\pi\rho})$.

compound	a_0 (Å)		V_0 (Å^3)		B_0 (GPa)	
Li	3.556 ± 0.005	[176]			13 ± 2	[176]
	3.477	[207]			12.8	[208]
Al	3.970 ± 0.014	[177]			65 ± 17	[177]
	4.022	[177]			81.3	[177]
GaAs	5.66 ± 0.05	[184]			79 ± 10	[184]
	5.642	[209]			77 ± 1	[210]
LiH	4.006	[211]			35.7 ± 0.1	[211]
	4.07 ± 0.01	[212]			32.2 ± 0.03	[212]
BN			11.812 ± 0.008	[135]	378 ± 3	[135]
			11.812 ± 0.001	[213]	395 ± 2	[213]
Mg			23.61 ± 0.04	[106]	31.2 ± 2.4	[106]
			23.24	[214]	36.8 ± 3.0	[215]
MgO	4.23	[216]			158	[216]
	4.213	[217]			160 ± 2	[217]
MgH_2			30.58 ± 0.06	[106]	39.5 ± 1.7	[106]
			30.49	[218]	—	
C	3.575 ± 0.002	[219]			437 ± 3	[219]
(diamond)	3.567	[188]			442 ± 4	[220]
Si	5.439 ± 0.003	[182]			103 ± 10	[182]
	5.430	[221]			99.2	[222]
SiO_2			37.6 ± 0.3	[223]	32 ± 6	[223]
(quartz)			37.69	[224]	34	[224]
FeO	4.324 ± 0.006	[119]			170 ± 10	[119]
	4.334	[225]			≈ 180	[226]

Table 2: Equilibrium lattice constants a_0, equilibrium volumes V_0 (per formula unit) and bulk moduli B_0 for a number of solids investigated with the QMC methods. The first line for each compound contains QMC predictions, the second line shows experimental data. Theoretical results for Li, Al and GaAs come from VMC simulations, the rest of the table corresponds to the DMC method.

5.3 Equations of state

The equilibrium volume V_0, the lattice constant a_0, and the bulk modulus $B_0 = V(\partial E/\partial V)|_{V=V_0}$ are among the most basic parameters characterizing elastic properties of a solid near the ambient conditions. Within QMC methods, these quantities are determined by evaluating the total energy at several volumes around V_0 and by fitting an appropriate model [227, 228] of the equation of state $E(V)$ through the acquired data, see figure 2 for an illustration. Results of this procedure for a wide range of solids are shown in table 2 together with the corresponding experimental data. As in the case of the cohesion energy discussed in the preceding section, the raw QMC numbers correspond to the static lattice and corrections due to the motion of nuclei may be needed to facilitate the comparison with experimentally measured quantities. Particular details about applied adjustments can be inspected in the original papers.

The data in table 2 demonstrate that the equilibrium geometries predicted by the QMC simulations are very good and all lie within 2 % from the experiments, in many cases within only a few tenths of a percent. The agreement is slightly worse for the bulk moduli, where errors of several percent are common and in a few instances the mean values of the Monte Carlo estimates deviate from the experimental numbers by more than 10 %. Note, however, that determination of the curvature of $E(V)$ near its minimum is impeded by the stochastic noise of the QMC energies and that the error bars on the less favourable results are relatively large.

Quantum Monte Carlo methods are not limited to the covalent solids listed in table 2. Investigation of the equation of state of solid neon [229] represents an application to a crystal bound by van der Waals forces. Although the shallowness of the minimum of the energy–volume curve in combination with the Monte Carlo noise did not allow to determine the lattice constant and the bulk modulus to a sufficient accuracy, the DMC equation of state was still substantially better than results obtained with LDA and GGA. This example together with a recent study of interlayer

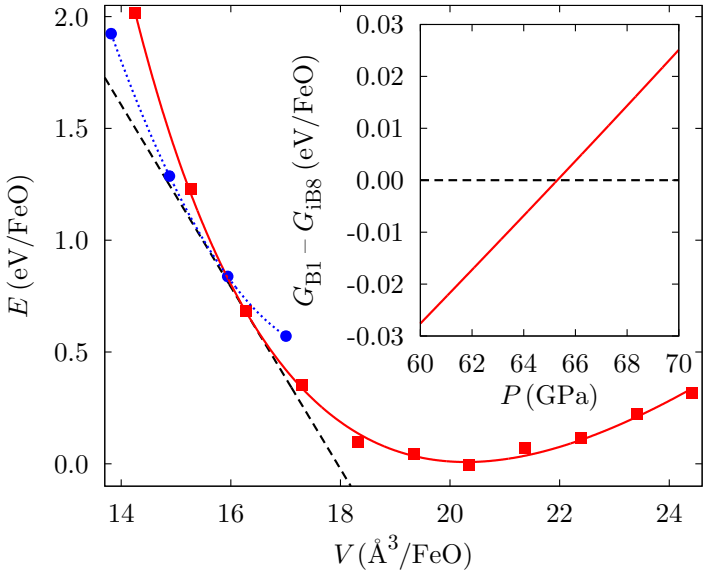

Figure 2: DMC total energies of the rock-salt (squares) and the NiAs (circles) phases of FeO. Statistical error bars are smaller than the symbol sizes. Lines are fits with the Murnaghan equation of state. Inset: Difference between the Gibbs potentials of the two phases at $T = 0$ K; its intercept with the x axis determines the transition pressure P_t. Adopted from [119].

binding in graphite [230] illustrate that the diffusion Monte Carlo method provides a fair description of dispersive forces already with the simple nodal structure defined by the single-determinantal Slater–Jastrow wave function. More accurate trial wave functions incorporating backflow correlations were employed to study van der Waals interactions between idealized metallic sheets and wires [231].

Calculations of the equations of state are by no means restricted to the vicinity of the equilibrium volume, and many of the references quoted in table 2 study the materials up to very high pressures. Such investigations are stimulated by open problems from Earth and planetary science as well as from other areas of materials physics. Combination of the equation of state with the pressure dependence of the Raman frequency [135, 219], both calculated from first principles with QMC, can provide a very accurate high-pressure calibration scale for use in experimental studies of condensed matter under extreme conditions [135].

5.4 Phase transitions

Theoretical understanding of structural phase transitions often necessitates a highly accurate description of the involved crystalline phases. Simple approximations are known to markedly fail in a number of instances due to significant changes in the bonding conditions across the transition. A classical example is the quartz–stishovite transition in silica (SiO_2), where LDA performs very poorly and GGA is needed to reconcile the DFT picture with experimental findings [232]. The diffusion Monte Carlo method has been employed to investigate pressure-induced phase transitions in Si [182], MgO [216], FeO [119] and SiO_2 [223].

A transition from the diamond structure to the β-tin phase in silicon was estimated to occur at $P_t = 16.5 \pm 0.5$ GPa [182], which lies outside the range of experimentally determined values 10.3–12.5 GPa (see [182] for compilation of experimental literature). Since the diamond structure is described very accurately with the DMC method as testified by the data in tables 1 and 2, it was suggested that the discrepancy is a manifestation of the fixed-node errors in the high-pressure β-tin phase. This view is supported by a recent calculation utilizing the so-called phaseless auxiliary-field QMC, a projector Monte Carlo method that shows smaller biases related to the fermion sign problem in this particular case and predicts the transition at 12.6 ± 0.3 GPa [233]. It should be noted, however, that the volume at which the transition occurs was fixed to its experimental value in this later study, whereas the approach pursued in [182] was entirely parameter-free.

In iron oxide (FeO), a transition from the rock-salt structure to a NiAs-based phase is experimentally observed to occur around 70 GPa at elevated temperatures [234] and to move to higher pressures exceeding 100 GPa when the temperature is lowered [235]. The DMC simulations summarized in figure 2 place the transition at $P_t = 65 \pm 5$ GPa [119]. This value represents a significant improvement over LDA and GGA that both find the NiAs structure more stable than the rock-salt phase at all volumes. The agreement with experiments is nevertheless not entirely satisfactory, since the DMC prediction corresponds to zero temperature where experimental observations suggest

stabilization of the rock-salt structure to higher pressures. Sizeable sensitivity of the transition pressure P_t to the choice of the one-particle orbitals in the Slater–Jastrow trial wave function was demonstrated in a subsequent study [157], but those wave functions that provided higher P_t also increased the total energies, and therefore represented poorer approximations of the electronic ground state. It remains to be determined, whether the discrepancy between the experiments and the DMC simulations is due to inaccuracies of the Slater–Jastrow nodes or if some physics not included in the investigation, for instance the inherently defective nature of the real FeO crystals, plays a significant role.

Investigations of phase transitions involving a liquid phase, such as melting, are considerably more involved due to a non-trivial motion of ions. An often pursued approach is a molecular dynamics simulation of ions subject to forces derived from the electronic ground state that is usually approximated within the density-functional theory. More accurate results would be achieved if the forces were calculated using quantum Monte Carlo methods instead. At present, this is generally not feasible due to excessive noise of the available force estimates [48]. Nevertheless, it was demonstrated that one can obtain an improved picture of the energetics of the simulated system when its electronic energy is evaluated with the aid of a QMC method while still following the ion trajectories provided by the DFT forces [236, 237].

5.5 Lattice defects

The energetics of point defects substantially influences high-temperature properties of crystalline materials. Experimental investigations of the involved processes are relatively difficult, and it would be very helpful if the electronic structure theory could provide dependable predictions. The role of electron correlations in point defects was investigated with the DMC method in silicon [206, 238] and in diamond [180]. The formation energies of selected self-interstitials in silicon were found about 1.5 eV larger than in LDA, whereas the formation energy of vacancies in diamond came out as approximately 1 eV smaller than in LDA. These differences represent 20–30 % of the formation energies and indicate that an improved account of electron correlations is necessary for accurate quantitative understanding of these phenomena.

Charged vacancies constituting the Schottky defect were investigated in MgO [239], and in this case the predictions of the DMC method differ only marginally from the results obtained within the local density approximation. The non-zero net charge of the supercells employed in these simulations represents an additional technical challenge in the form of increased finite-size effects that require a modification of some of the size extrapolation techniques discussed in section 3 [240, 241].

5.6 Surface phenomena

Materials surfaces are fascinating systems from the point of view of electronic structure and correlation effects. The vacuum boundary condition provides surface atoms with more space to relax their positions and surface electronic states enable the electronic structure to develop features which cannot form in the periodic bulk. This leads to a plethora of surface reconstruction possibilities with perhaps the most studied paradigmatic case of 7×7 Si(111) surface reconstruction. Seemingly, QMC methods should be straightforward to apply to these systems, similarly to the three-dimensional periodic solids. However, mainly technical reasons make such calculations quite difficult. There are basically two possibilities how to model a surface. One option is to use a two-dimensional periodic slab geometry which requires certain minimal slab thickness in order to accurately represent the bulk environment for the surface layers on both sides. The resulting simulation cells end up quite large making many such simulations out of reach at present. The other option is to use a cluster with appropriate termination that mimics the bonding pattern of the bulk atoms. This strategy assumes that the termination does not affect the surface geometries in a substantial manner. Moreover, it is applicable only to insulating systems. Given these difficulties, the QMC simulations of surfaces are rare and this research area awaits to be explored in future.

The simplest possible model for investigation of surface physics is the surface of the homogeneous electron gas that has been studied by DFT as well as QMC methods. The first QMC calculations [243] were later found to be biased due to complications arising from finite-size effects, especially due to different scaling of finite-size corrections for bulk and surface. Once these issues have been properly taken into account by Wood and coworkers [242], the QMC results have exhibited trends that were consistent with DFT and RPA methods which are expected to perform reasonably well for this model system (see table 3).

Applications to real materials surfaces are still very few. The cluster model was used in calculations of Si(001) surface by Healy *et al.* [244] with the goal of elucidating a long-standing puzzle in reconstruction geometry of this surface, which exhibits regularly spaced rows of Si-Si dimers. The dimers could take

Table 3: Comparison of the surface energies (in erg cm^{-2}) of the homogeneous electron gas calculated by a number of electronic structure methods [242]. The DMC calculations were done with the LDA orbitals in the trial wave functions.

r_s	LDA	GGA	DMC	RPA
2.07	−608.2	−690.6	-563 ± 45	−517
2.30	−104.0	−164.1	-82 ± 27	−34
2.66	170.6	133.0	179 ± 13	216
3.25	221.0	201.2	216 ± 8	248
3.94	168.4	158.1	175 ± 8	182

two possible conformations: They can be either positioned symmetrically or form an alternating buckling in a zig-zag fashion. While experiments suggested the buckled geometry as the low-temperature ground state, theoretical calculations produced conflicting results, in which various methods favoured one or the other structure. The QMC calculations [244] concluded that the buckled geometry is lower by about 0.2 eV/Si_2. This problem was studied with QMC methodology also by Bokes and coworkers [245] who found that several systematic errors (such as uncertainty of geometries in cluster models and pseudopotential biases) added to about 0.2 eV, and therefore prevented unequivocal determination of the most stable geometry. This conclusion corroborated the experimental findings which suggested that at temperatures above 100 K the distinct features of buckling were largely washed out and indicated that the effect is energetically very small. Very recently, the QMC study of this system has been repeated by Jordan and coworkers [246] with the conclusion that the buckled structure is lower by about 0.1 eV/Si_2 and that the highest level correlated basis set method which they used (CASPT3) is consistent with this finding. It was also clear that once the correlations were taken into account, the energy differences between the competing surface reconstruction patterns were becoming very small. This brings the calculations closer to reality, where the two structures could be within a fraction of 0.1 eV/Si_2 as suggested by experiments.

Perhaps the most realistic QMC calculations of surfaces have been done on LiH and MgO surfaces by the group of Alfè and Gillan [211, 247] who compared predictions of several DFT functionals with the fixed-node DMC method. The results showed significant differences between various exchange-correlation functionals. For the MgO(100) surface the best agreement with QMC results was found for the LDA functional, while for the LiH surface the closest agreement between QMC and DFT predictions was found for particular GGA functionals.

Clearly, more applications are needed to assess the effectiveness of QMC approaches for investigation of surface physics. As we have already mentioned, the surfaces represent quite challenging systems for QMC methods. Nevertheless, we expect more applications to appear in the future since the field is very rich in variety of correlation effects that are difficult to capture by more conventional methods.

5.7 Excited states

The VMC and the fixed-node DMC methods both build on the variational principle, and they therefore seem to be applicable exclusively to the ground-state properties. Nevertheless, the variational principle can be symmetry constrained, in which case the algorithms search for the lowest lying eigenstate within the given symmetry class (provided, in the case of the DMC method, that the eigenstate is non-degenerate [62]), and thus enable access to selected excited states.

Excitation energies in solids are calculated as differences between the total energy obtained for the ground state and for the excited state. It is a computationally demanding procedure since the stochastic fluctuations of the total energies are proportional to the number of electrons in the simulation cell, whereas the excitation energy is an intensive quantity. Trial wave functions for excited states are formed by modifying the determinantal part of the ground-state Slater–Jastrow wave function such that an occupied orbital in the ground-state determinant is replaced by a virtual orbital. This substitution corresponds to an optical absorption experiment where an electron is excited from the valence band into the conduction band. The fact that both the original occupied orbital and the new virtual orbital necessarily belong to the same K point restricts the types of excitations that can be studied, since only a limited number of k points from the primitive cell fold to the given K point of the simulation cell, recall equations (55)–(57). Clearly, the larger the simulation cell, the finer mapping out of excitations can be performed.

Averaging over twisted boundary conditions (section 3.1) is not applicable to the calculations of the excitation energies, since both the ground state and the excited state are fixed to a single K point. This is not a significant issue, since finite-size effects tend to cancel very efficiently in the differences of the total energies calculated at the same K point.

compound	DMC	experiment
MnO	4.8 ± 0.2 [248]	3.9 ± 0.4 [249]
FeO	2.8 ± 0.3 [119]	≈ 2.4 [250]

Table 4: Band gaps (in eV) of Mott insulators MnO and FeO calculated with the fixed-node DMC method. Experimental data are provided for comparison.

DMC simulations following the outlined recipe were utilized to estimate the band gap in solid nitrogen [251] and in transition-metal oxides FeO [119] and MnO [248]. The gaps calculated for the two strongly correlated oxides are compared with experimental data in table 4. The ratio of the FeO and MnO gaps is reproduced quite well, but the DMC gaps themselves are somewhat overestimated, likely due to inaccuracies of the trial wave functions used for the excited states. A large number of excitations were calculated in silicon [252] and in diamond [145, 253], and the obtained data were used to map, albeit sparsely, the entire band structure. In these weakly correlated solids the agreement with experiments is very good. Recently, a pressure-induced insulator–metal transition was investigated in solid helium by calculating the evolution of the band gap with compression [254]. As illustrated in figure 3 (*copyrighted material; not available in this version; see figure 1 in [254]*), the DMC band gaps were found to practically coincide with the gaps calculated with the *GW* method.

5.8 BCS–BEC crossover

The repulsive Coulomb interaction considered so far is not the only source of non-trivial many-body effects in the electronic structure of solids. A weak attractive interaction among electrons is responsible for a very fundamental phenomenon—the electronic states in the vicinity of the Fermi level rearrange into bosonic Cooper pairs that condense and give rise to superconductivity. The ground state of the system can be described by the BCS wave function Ψ_{BCS} discussed earlier in section 4.4 [164]. The Cooper pair is an entity that has a meaning only as a constituent of Ψ_{BCS}. In order to form an isolated two-electron bound state, some minimal strength of the two-body potential is needed in three dimensions, whereas the Cooper instability itself occurs for arbitrarily weak attraction. When the interaction is very strong, the composite bosons formed as the two-electron bound states indeed exist and undergo the Bose–Einstein condensation (BEC). It turns out that a mean-field description of both the BCS and BEC limits leads to the same form of the many-body wave function, which indicates that the interacting fermionic system is likely to continuously evolve from one limit to the other when the interaction strength is gradually changed [256–258]. A large amount of research activity aimed at detailed understanding of this physics was stimulated by the possibility to realize the BCS–BEC crossover in experiments with optically trapped ultra-cold atoms [259].

In a dilute Fermi gas with short-ranged spherically symmetric inter-particle potentials, the interactions are fully characterized by a single parameter, the two-body scattering length a. The system is interpolated from the BCS regime to the BEC limit by varying $1/a$ from $-\infty$ to ∞. In experiments, this is achieved by tuning across the Feshbach resonance with the aid of an external magnetic field. Particularly intriguing is the quantum state of an unpolarized homogeneous gas at the resonance itself, where the scattering length diverges ($1/a = 0$). The only relevant length scale remaining in the problem in this case is the inverse of the Fermi wave vector $1/k_{\mathrm{F}}$, and all ground-state properties should therefore be universal functions of the Fermi energy E_{F}. Since there is only a single length scale, the system is said to be in the unitary limit. The total energy can be written as

$$E = \xi E_{\mathrm{free}} = \xi \, \frac{3}{5} E_{\mathrm{F}} \,, \tag{62}$$

where E_{free} denotes the energy of a non-interacting system and ξ is a universal parameter. The universality of ξ is illustrated in figure 4 that shows the ratio E/E_{free} as a function of the interaction strength calculated for three different particle densities using the diffusion Monte Carlo method with the trial wave function of the BCS–Jastrow form. All three curves indeed intersect at $1/a = 0$ with the parameter ξ estimated as 0.42 ± 0.01 [166, 260–262]. The energy calculated with the fermionic nodes fixed by the Slater–Jastrow wave function is considerably higher and would lead to $\xi \approx 0.54$ [166], which underlines the significance of particle pairing in this system.

A further insight into the formation of the Cooper pairs is provided by evaluation of the condensate fraction that can be estimated from the off-diagonal long-range order occurring in the two-particle density matrix [263]. The condensate fraction α is given as

$$\alpha = \frac{N}{2} \lim_{r \to \infty} \rho^{\mathrm{P}}_{2\uparrow\downarrow}(r) \tag{63}$$

and the so-called projected two-particle density matrix

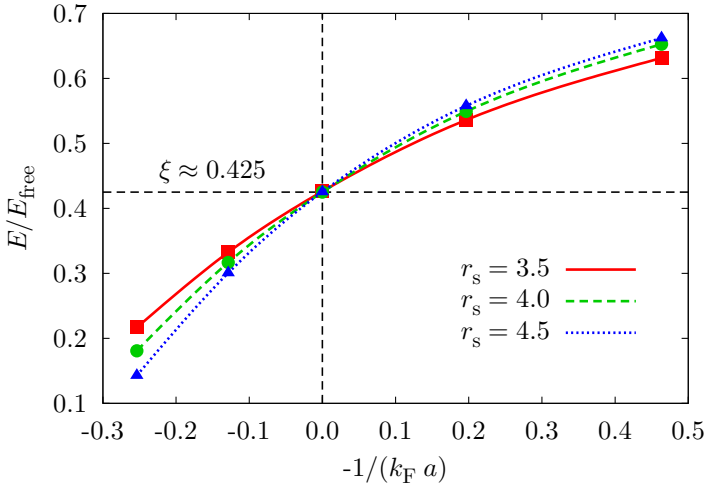

Figure 4: Fixed-node DMC energies of 38 fermions in a cubic box with the periodic boundary conditions plotted as a function of interaction strength. BEC regime is on the left, BCS limit on the right. Shown are three particle densities ρ characterized by the dimensionless parameter $r_{\rm s}$ defined in section 5.1. The simulations employed BCS–Jastrow trial wave function. Statistical error bars are smaller than the symbol sizes. Data taken from [255].

$\rho^{\rm P}_{2\uparrow\downarrow}$ is [264]

$$\rho^{\rm P}_{2\uparrow\downarrow}(\boldsymbol{r}) = \frac{1}{4\pi}\int \mathrm{d}\Omega_{\boldsymbol{r}} \int \mathrm{d}^{3N}\mathcal{R} \times \Psi^*(\boldsymbol{r}_1+\boldsymbol{r}, \boldsymbol{r}_2+\boldsymbol{r}, \boldsymbol{r}_3, \ldots, \boldsymbol{r}_N) \times \Psi(\boldsymbol{r}_1, \boldsymbol{r}_2, \boldsymbol{r}_3, \ldots, \boldsymbol{r}_N)\,, \qquad (64)$$

where $\boldsymbol{r}_1$ corresponds to the spin-up state and $\boldsymbol{r}_2$ to the spin-down state. The evolution of α with interaction strength calculated with the DMC method [265] is shown in figure 5 (*copyrighted material; not available in this version; see figure 4 in [265]*). It is found that approximately half of the particles participates in pairing in the unitary regime and this fraction quickly decreases towards the BCS limit, where only states in the immediate vicinity of the Fermi level contribute to the Cooper pair formation. Note that the condensate fraction vanishes if the Slater–Jastrow form is used in place of the trial wave function.

The diffusion Monte Carlo simulations were used to study also the total energy and the particle density profile in the unitary Fermi gas subject to a harmonic confining potential [266–268]. Due to the lowered symmetry compared to the homogeneous calculations referred above, the system sizes were more limited. To extrapolate the findings to a larger number of particles, a density functional theory fitted to the DMC data can be employed [269].

6 Concluding remarks

In this article we have attempted to provide an overview of selected quantum Monte Carlo methods that facilitate calculation of various properties of correlated quantum systems to a very high accuracy. Particular attention has been paid to technical details pertaining to applications of the methodology to extended systems such as bulk solids. We hope that we have been able to demonstrate that the QMC methods, thanks to their accuracy and a wide range of applicability, represent a powerful and valuable alternative to more traditional ab initio computational tools.

Acknowledgments

We thank G. E. Astrakharchik and B. Militzer for providing their data, and K. M. Rasch for suggestions to the manuscript. J. K. would like to acknowledge financial support by the Alexander von Humboldt foundation during preparation of the article. Support of L. M. research by NSF EAR-05301110, DMR-0804549 and OCI-0904794 grants and by DOD/ARO and DOE/LANL DOE-DE-AC52-06NA25396 grants is gratefully acknowledged. We acknowledge also allocations at ORNL through INCITE and CNMS initiatives as well as allocations at NSF NCSA and TACC centers.

[1] Dirac P A M 1929 Quantum mechanics of many-electron systems *Proc. R. Soc. Lond. A* **123** 714–733

[2] Metropolis N and Ulam S 1949 The Monte Carlo method *J. Am. Stat. Assoc.* **44** 335–341

[3] Metropolis N, Rosenbluth A W, Rosenbluth M N, Teller A H and Teller E 1953 Equation of state calculations by fast computing machines *J. Chem. Phys.* **21** 1087–1092

[4] Kalos M H 1962 Monte Carlo calculations of the ground state of three- and four-body nuclei *Phys. Rev.* **128** 1791–1795

[5] McMillan W L 1965 Ground state of liquid He^4 *Phys.*

Rev. **138** A442–A451

[6] Kalos M H, Levesque D and Verlet L 1974 Helium at zero temperature with hard-sphere and other forces *Phys. Rev. A* **9** 2178–2195

[7] Whitlock P A, Ceperley D M, Chester G V and Kalos M H 1979 Properties of liquid and solid ^{4}He *Phys. Rev. B* **19** 5598–5633

[8] Ceperley D, Chester G V and Kalos M H 1977 Monte Carlo simulation of a many-fermion study *Phys. Rev. B* **16** 3081–3099

[9] Lee M A, Schmidt K E, Kalos M H and Chester G V 1981 Green's function Monte Carlo method for liquid ^{3}He *Phys. Rev. Lett.* **46** 728–731

[10] Ceperley D 1978 Ground state of the fermion one-component plasma: A Monte Carlo study in two and three dimensions *Phys. Rev. B* **18** 3126–3138

[11] Ceperley D M and Alder B J 1980 Ground state of the electron gas by a stochastic method *Phys. Rev. Lett.* **45** 566–569

[12] Anderson J B 1975 A random-walk simulation of the Schrödinger equation: H_3^+ *J. Chem. Phys.* **63** 1499–1502

[13] Anderson J B 1976 Quantum chemistry by random walk. H ^2P, H_3^+ D_{3h} $^1A_1'$, H_2 $^3\Sigma_u^+$, H_4 $^1\Sigma_g^+$, Be ^1S *J. Chem. Phys.* **65** 4121–4127

[14] Landau D P and Binder K 2009 *A guide to Monte-Carlo simulations in statistical physics* (Cambridge University Press, Cambridge)

[15] Wagner L K, Bajdich M and Mitas L 2009 QWalk: A quantum Monte Carlo program for electronic structure *J. Comput. Phys.* **228** 3390–3404 `http://www.qwalk.org/`

[16] QMCPACK `http://qmcpack.cmscc.org/`

[17] CHAMP `http://pages.physics.cornell.edu/~cyrus/champ.html`

[18] Needs R J, Towler M D, Drummond N D and López Ríos P 2009 *CASINO version 2.3 user manual* (University of Cambridge, Cambridge, UK) `http://www.tcm.phy.cam.ac.uk/~mdt26/casino2.html`

[19] QMcBeaver `http://qmcbeaver.sourceforge.net/`

[20] Davies C T H *et al.* 2004 High-precision lattice QCD confronts experiment *Phys. Rev. Lett.* **92** 022001

[21] Dürr S, Fodor Z, Frison J, Hoelbling C, Hoffmann R, Katz S D, Krieg S, Kurth T, Lellouch L, Lippert T, Szabo K K and Vulvert G 2008 Ab initio determination of light hadron masses *Science* **322** 1224–1227

[22] Hartree D R 1928 The wave mechanics of an atom with a non-Coulomb central field. Part I. Theory and methods *Proc. Cambridge Philos. Soc.* **24** 89–110

[23] Fock V 1930 Näherungsmethode zur Lösung des quantenmechanischen Mehrkörperproblems *Z. Phys.* **61** 126–148

[24] Pauli W 1925 Über den Zusammenhang des Abschlusses der Elektronengruppen im Atom mit der Komplexstruktur der Spektren *Z. Phys.* **31** 765–783

[25] Pauli W 1927 Zur Quantenmechanik des magnetischen Elektrons *Z. Phys.* **43** 601–623

[26] Slater J C 1930 Note on Hartree's method *Phys. Rev.* **35** 210–211

[27] Bloch F 1929 Über die Quantenmechanik der Elektronen in Kristallgittern *Z. Phys.* **52** 555–600

[28] Wigner E and Seitz F 1933 On the constitution of metallic sodium *Phys. Rev.* **43** 804–810

[29] Wigner E and Seitz F 1934 On the constitution of metallic sodium. II *Phys. Rev.* **46** 509–524

[30] Hohenberg P and Kohn W 1964 Inhomogeneous electron gas *Phys. Rev.* **136** B864–B871

[31] Kohn W and Sham L J 1965 Self-consistent equations including exchange and correlation effects *Phys. Rev.* **140** A1133–A1138

[32] von Barth U and Hedin L 1972 A local exchange-correlation potential for the spin polarized case. I *J. Phys. C: Solid State Phys.* **5** 1629–1642

[33] Langreth D C and Mehl M J 1983 Beyond the local-density approximation in calculations of ground-state electronic properties *Phys. Rev. B* **28** 1809–1834

[34] Perdew J P, Burke K and Ernzerhof M 1996 Generalized gradient approximation made simple *Phys. Rev. Lett.* **77** 3865–3868

[35] Perdew J P and Zunger A 1981 Self-interaction correction to density-functional approximations for many-electron systems *Phys. Rev. B* **23** 5048–5079

[36] Anisimov V I, Zaanen J and Andersen O K 1991 Band theory and Mott insulators: Hubbard U instead of Stoner I *Phys. Rev. B* **44** 943–954

[37] Kümmel S and Kronik L 2008 Orbital-dependent density functionals: Theory and applications *Rev. Mod. Phys.* **80** 3–60

[38] Kurth S, Perdew J P and Blaha P 1999 Molecular and solid-state tests of density functional approximations: LSD, GGAs, and meta-GGAs *Int. J. Quant. Chem.* **75** 889–909

[39] Sousa S F, Fernandes P A and Ramos M J 2007 General performance of density functionals *J. Phys. Chem. A* **111** 10439–10452

[40] Szabo A and Ostlund N S 1989 *Modern Quantum Chemistry: Introduction to Advanced Electronic Structure Theory* (Dover, New York)

[41] Hastings W K 1970 Monte Carlo sampling methods using Markov chains and their applications *Biometrika* **57** 97–109

[42] Trail J R 2008 Heavy-tailed random error in quantum Monte Carlo *Phys. Rev. E* **77** 016703

[43] Flyvbjerg H and Petersen H G 1989 Error estimates on averages of correlated data *J. Chem. Phys.* **91** 461–466

[44] Assaraf R and Caffarel M 1999 Zero-variance princi-

ple for Monte Carlo algorithms *Phys. Rev. Lett.* **83** 4682–4685

[45] Assaraf R and Caffarel M 2000 Computing forces with quantum Monte Carlo *J. Chem. Phys.* **113** 4028–4034

[46] Assaraf R, Caffarel M and Scemama A 2007 Improved Monte Carlo estimators for the one-body density *Phys. Rev. E* **75** 035701(R)

[47] Toulouse J, Assaraf R and Umrigar C J 2007 Zero-variance zero-bias quantum Monte Carlo estimators of the spherically and system-averaged pair density *J. Chem. Phys.* **126** 244112

[48] Badinski A, Haynes P D, Trail J R and Needs R J 2010 Methods for calculating forces within quantum Monte Carlo simulations *J. Phys.: Condens. Matter* **22** 074202

[49] Grimm R C and Storer R G 1971 Monte-Carlo solution of Schrödinger's equation *J. Comp. Phys.* **7** 134–156

[50] Hammond B L, Lester Jr W A and Reynolds P J 1994 *Monte Carlo Methods in Ab Initio Quantum Chemistry* (World Scientific, Singapore)

[51] Foulkes W M C, Mitas L, Needs R J and Rajagopal G 2001 Quantum Monte Carlo simulations of solids *Rev. Mod. Phys.* **73** 33–83

[52] Bressanini D and Reynolds P J 2005 Unexpected symmetry in the nodal structure of the He atom *Phys. Rev. Lett.* **95** 110201

[53] Bressanini D, Morosi G and Tarasco S 2005 An investigation of nodal structures and the construction of trial wave functions *J. Chem. Phys.* **123** 204109

[54] Bajdich M, Mitas L, Drobný G and Wagner L K 2005 Approximate and exact nodes of fermionic wavefunctions: Coordinate transformations and topologies *Phys. Rev. B* **72** 075131

[55] Klein D J and Pickett H M 1976 Nodal hypersurfaces and Anderson's random-walk simulation of the Schrödinger equation *J. Chem. Phys.* **64** 4811–4812

[56] Ceperley D M 1991 Fermion nodes *J. Stat. Phys.* **63** 1237–1267

[57] Mitas L 2006 Structure of fermion nodes and nodal cells *Phys. Rev. Lett.* **96** 240402

[58] Mitas L 2006 Fermion nodes and nodal cells of noninteracting and interacting fermions arXiv:cond-mat/0605550

[59] Bajdich M and Mitas L 2009 Electronic structure quantum Monte Carlo *Acta Physica Slovaca* **59** 81–168

[60] Moskowitz J W, Schmidt K E, Lee M A and Kalos M H 1982 A new look at correlation energy in atomic and molecular systems. II. The application of the Green's function Monte Carlo method to LiH *J. Chem. Phys.* **77** 349–355

[61] Reynolds P J, Ceperley D M, Alder B J and Lester Jr W A 1982 Fixed-node quantum Monte Carlo for molecules *J. Chem. Phys.* **77** 5593–5603

[62] Foulkes W M C, Hood R Q and Needs R J 1999 Symmetry constraints and variational principles in diffusion quantum Monte Carlo calculations of excited-state energies *Phys. Rev. B* **60** 4558–4570

[63] Manten S and Lüchow A 2001 On the accuracy of the fixed-node diffusion quantum Monte Carlo method *J. Chem. Phys.* **115** 5362

[64] Grossman J C 2002 Benchmark quantum Monte Carlo calculations *J. Chem. Phys.* **117** 1434–1440

[65] Ortiz G, Ceperley D M and Martin R M 1993 New stochastic method for systems with broken time-reversal symmetry: 2D fermions in a magnetic field *Phys. Rev. Lett.* **71** 2777–2780

[66] Trotter H F 1959 On the product of semi-groups of operators *Proc. Am. Math. Soc.* **10** 545–551

[67] Suzuki M 1985 Decomposition formulas of exponential operators and Lie exponentials with some applications to quantum mechanics and statistical physics *J. Math. Phys.* **26** 601–612

[68] Caffarel M and Claverie P 1988 Development of a pure diffusion quantum Monte Carlo method using a full generalized Feynman–Kac formula. I. Formalism *J. Chem. Phys.* **88** 1088–1099

[69] Ceperley D M and Bernu B 1988 The calculation of excited state properties with quantum Monte Carlo *J. Chem. Phys.* **89** 6316–6328

[70] Assaraf R, Caffarel M and Khelif A 2000 Diffusion Monte Carlo methods with a fixed number of walkers *Phys. Rev. E* **61** 4566–4575

[71] Caffarel M and Claverie P 1988 Development of a pure diffusion quantum Monte Carlo method using a full generalized Feynman–Kac formula. II. Applications to simple systems *J. Chem. Phys.* **88** 1100–1109

[72] Flad H and Dolg M 1997 Probing the accuracy of pseudopotentials for transition metals in quantum Monte Carlo calculations *J. Chem. Phys.* **107** 7951–7959

[73] Schautz F and Flad H J 1999 Quantum Monte Carlo study of the dipole moment of CO *J. Chem. Phys.* **110** 11700–11707

[74] Umrigar C J, Nightingale M P and Runge K J 1993 A diffusion Monte Carlo algorithm with very small time-step errors *J. Chem. Phys.* **99** 2865–2890

[75] Nemec N 2010 Diffusion Monte Carlo: Exponential scaling of computational cost for large systems *Phys. Rev. B* **81** 035119

[76] Hetherington J H 1984 Observations on the statistical iteration of matrices *Phys. Rev. A* **30** 2713–2719

[77] Buonaura M C and Sorella S 1998 Numerical study of the two-dimensional Heisenberg model using a Green function Monte Carlo technique with a fixed number of walkers *Phys. Rev. B* **57** 11446–11456

[78] Jones A, Thompson A, Crain J, Müser M H and Martyna G J 2009 Norm-conserving diffusion Monte Carlo method and diagrammatic expansion of interacting Drude oscillators: Application to solid xenon *Phys. Rev. B* **79** 144119

[79] Baroni S and Moroni S 1999 Reptation quantum Monte Carlo: A method for unbiased ground-state averages and imaginary-time correlations *Phys. Rev. Lett.* **82** 4745–4748

[80] Moroni S private communication

[81] Liu K S, Kalos M H and Chester G V 1974 Quantum hard spheres in a channel *Phys. Rev. A* **10** 303–308

[82] Barnett R N, Reynolds P J and Lester Jr W A 1991 Monte Carlo algorithms for expectation values of coordinate operators *J. Comput. Phys.* **96** 258–276

[83] Pierleoni C and Ceperley D M 2005 Computational methods in coupled electron-ion Monte Carlo simulations *ChemPhysChem* **6** 1872–1878

[84] Yuen W K, Oblinsky D G, Giacometti R D and Rothstein S M 2009 Improving reptation quantum Monte Carlo *Int. J. Quant. Chem.* **109** 3229–3234

[85] Gaudoin R and Pitarke J M 2007 Hellman–Feynman operator sampling in diffusion Monte Carlo calculations *Phys. Rev. Lett.* **99** 126406

[86] Gaudoin R and Pitarke J M 2010 Efficient method for the quantum Monte Carlo evaluation of the static density response function of a many-electron system *Phys. Rev. B* **81** 245116

[87] Carlson J 1987 Green's function Monte Carlo study of light nuclei *Phys. Rev. C* **36** 2026–2033

[88] Pudliner B S, Pandharipande V R, Carlson J, Pieper S C and Wiringa R B 1997 Quantum Monte Carlo calculations of nuclei with $A \leq 7$ *Phys. Rev. C* **56** 1720–1750

[89] Schmidt K E and Fantoni S 1999 A quantum Monte Carlo method for nucleon systems *Physics Letters B* **446** 99–103

[90] Sarsa A, Fantoni S, Schmidt K E and Pederiva F 2003 Neutron matter at zero temperature with an auxiliary field diffusion Monte Carlo method *Phys. Rev. C* **68** 024308

[91] Ambrosetti A, Pederiva F, Lipparini E and Gandolfi S 2009 Quantum Monte Carlo study of the two-dimensional electron gas in presence of Rashba interaction *Phys. Rev. B* **80** 125306

[92] Ceperley D M 1986 The statistical error of Green's function Monte Carlo *J. Stat. Phys.* **43** 815–826

[93] Hammond B L, Reynolds P J and Lester W A 1987 Valence quantum Monte Carlo with ab initio effective core potentials *J. Chem. Phys.* **87** 1130–1136

[94] Ma A, Drummond N D, Towler M D and Needs R J 2005 All-electron quantum Monte Carlo calculations for the noble gas atoms He to Xe *Phys. Rev. E* **71** 066704

[95] Lee Y, Kent P R C, Towler M D, Needs R J and Rajagopal G 2000 Pseudopotentials for correlated-electron calculations *Phys. Rev. B* **62** 13347–13355

[96] Ovcharenko I, Aspuru-Guzik A and Lester Jr W A 2001 Soft pseudopotentials for efficient quantum Monte Carlo calculations: From Be to Ne and Al to Ar *J. Chem. Phys.* **114** 7790–7794

[97] Trail J R and Needs R J 2004 Norm-conserving Hartree–Fock pseudopotentials and their asymptotic behavior *J. Chem. Phys.* **122** 014112

[98] Trail J R and Needs R J 2005 Smooth relativistic Hartree–Fock pseudopotentials for H to Ba and Lu to Hg *J. Chem. Phys.* **122** 174109

[99] Burkatzki M, Filippi C and Dolg M 2007 Energy-consistent pseudopotentials for quantum Monte Carlo calculations *J. Chem. Phys.* **126** 234105

[100] Burkatzki M, Filippi C and Dolg M 2008 Energy-consistent small-core pseudopotentials for 3d-transition metals adapted to quantum Monte Carlo calculations *J. Chem. Phys.* **129** 164115

[101] Fahy S, Wang X W and Louie S G 1990 Variational quantum Monte Carlo nonlocal pseudopotential approach to solids: Formulation and application to diamond, graphite, and silicon *Phys. Rev. B* **42** 3503–3522

[102] Mitáš L, Shirley E L and Ceperley D M 1991 Nonlocal pseudopotentials and diffusion Monte Carlo *J. Chem. Phys.* **95** 3467–3475

[103] Hurley M M and Christiansen P A 1987 Relativistic effective potentials in quantum Monte Carlo calculations *J. Chem. Phys.* **86** 1069–1070

[104] ten Haaf D F B, van Bemmel H J M, van Leeuwen J M J, van Saarloos W and Ceperley D M 1995 Proof for an upper bound in fixed-node Monte Carlo for lattice fermions *Phys. Rev. B* **51** 13039–13045

[105] Casula M 2006 Beyond the locality approximation in the standard diffusion Monte Carlo method *Phys. Rev. B* **74** 161102(R)

[106] Pozzo M and Alfè D 2008 Structural properties and enthalpy of formation of magnesium hydride from quantum Monte Carlo calculations *Phys. Rev. B* **77** 104103

[107] Casula M, Moroni S, Sorella S and Filippi C 2010 Size-consistent variational approaches to non-local pseudopotentials: Standard and lattice regularized diffusion Monte Carlo methods revisited *J. Chem. Phys.* **132** 154113

[108] Rajagopal G, Needs R J, Kenny S, Foulkes W M C and James A 1994 Quantum Monte Carlo calculations for solids using special k points methods *Phys. Rev. Lett.* **73** 1959–1962

[109] Rajagopal G, Needs R J, James A, Kenny S D and Foulkes W M C 1995 Variational and diffusion quantum Monte Carlo calculations at nonzero wave vectors: Theory and application to diamond-structure

germanium *Phys. Rev. B* **51** 10591–10600

[110] Lin C, Zong F H and Ceperley D M 2001 Twist-averaged boundary conditions in continuum quantum Monte Carlo algorithms *Phys. Rev. E* **64** 016702

[111] Tinka Gammel J, Campbell D K and Loh Jr E Y 1993 Extracting infinite system properties from finite size clusters: "Phase randomization/boundary condition averaging" *Synthetic Metals* **55–57** 4437–4442

[112] de Leeuw S W, Perram J W and Smith E R 1980 Simulation of electrostatic systems in periodic boundary conditions. I. Lattice sums and dielectric constants *Proc. R. Soc. London, Ser. A* **373** 27–56

[113] Fraser L M, Foulkes W M C, Rajagopal G, Needs R J, Kenny S D and Williamson A J 1996 Finite-size effects and Coulomb interactions in quantum Monte Carlo calculations for homogeneous systems with periodic boundary conditions *Phys. Rev. B* **53** 1814–1832

[114] Allen M P and Tildesley D J 1989 *Computer Simulation of Liquids* (Oxford University Press, Oxford)

[115] Natoli V and Ceperley D M 1995 An optimized method for treating long-range potentials *J. Comput. Phys.* **117** 171–178

[116] Rajagopal G and Needs R J 1994 An optimized Ewald method for long-ranged potentials *J. Comput. Phys.* **115** 399–405

[117] Ceperley D M and Alder B J 1987 Ground state of solid hydrogen at high pressures *Phys. Rev. B* **36** 2092–2106

[118] Pozzo M and Alfè D 2008 Hydrogen dissociation on Mg(0001) studied via quantum Monte Carlo calculations *Phys. Rev. B* **78** 245313

[119] Kolorenč J and Mitas L 2008 Quantum Monte Carlo calculations of structural properties of FeO under pressure *Phys. Rev. Lett.* **101** 185502

[120] Williamson A J, Rajagopal G, Needs R J, Fraser L M, Foulkes W M C, Wang Y and Chou M Y 1997 Elimination of Coulomb finite-size effects in quantum many-body simulations *Phys. Rev. B* **55** R4851–R4854

[121] Chiesa S, Ceperley D M, Martin R M and Holzmann M 2006 Finite-size error in many-body simulations with long-range interactions *Phys. Rev. Lett.* **97** 076404

[122] Bohm D and Pines D 1953 A collective description of electron interactions: III. Coulomb interactions in a degenerate electron gas *Phys. Rev.* **92** 609–625

[123] Drummond N D, Needs R J, Sorouri A and Foulkes W M C 2008 Finite-size errors in continuum quantum Monte Carlo calculations *Phys. Rev. B* **78** 125106

[124] Kwee H, Zhang S and Krakauer H 2008 Finite-size correction in many-body electronic structure calculations *Phys. Rev. Lett.* **100** 126404

[125] Kent P R C, Hood R Q, Williamson A J, Needs R J, Foulkes W M C and Rajagopal G 1999 Finite-size errors in quantum many-body simulations of extended systems *Phys. Rev. B* **59** 1917–1929

[126] Maezono R, Towler M D, Lee Y and Needs R J 2003 Quantum Monte Carlo study of sodium *Phys. Rev. B* **68** 165103

[127] Nightingale M P and Melik-Alaverdian V 2001 Optimization of ground- and excited-state wave functions and van der Waals clusters *Phys. Rev. Lett.* **87** 043401

[128] Umrigar C J and Filippi C 2005 Energy and variance optimization of many-body wave functions *Phys. Rev. Lett.* **94** 150201

[129] Toulouse J and Umrigar C J 2007 Optimization of quantum Monte Carlo wave functions by energy minimization *J. Chem. Phys.* **126** 084102

[130] Umrigar C J, Toulouse J, Filippi C, Sorella S and Hennig R G 2007 Alleviation of the fermion-sign problem by optimization of many-body wave functions *Phys. Rev. Lett.* **98** 110201

[131] Kato T 1957 On the eigenfunctions of many-particle systems in quantum mechanics *Commun. Pure Appl. Math.* **10** 151–177

[132] Pack R T and Brown W B 1966 Cusp conditions for molecular wavefunctions *J. Chem. Phys.* **45** 556–559

[133] Jastrow R 1955 Many-body problem with strong forces *Phys. Rev.* **98** 1479–1484

[134] Ma A, Towler M D, Drummond N D and Needs R J 2005 Scheme for adding electron-nucleus cusps to Gaussian orbitals *J. Chem. Phys.* **122** 224322

[135] Esler K P, Cohen R E, Militzer B, Kim J, Needs R and Towler M 2010 Fundamental high-pressure calibration from all-electron quantum Monte Carlo calculations *Phys. Rev. Lett.* **104** 185702

[136] Drummond N D, Towler M D and Needs R J 2004 Jastrow correlation factor for atoms, molecules, and solids *Phys. Rev. B* **70** 235119

[137] Umrigar C J, Wilson K G and Wilkins J W 1988 Optimized trial wave functions for quantum Monte Carlo calculations *Phys. Rev. Lett.* **60** 1719–1722

[138] Schmidt K E and Moskowitz J W 1990 Correlated Monte Carlo wave functions for the atoms He through Ne *J. Chem. Phys.* **93** 4172–4178

[139] Umezawa N and Tsuneyuki S 2003 Transcorrelated method for electronic systems coupled with variational Monte Carlo calculation *J. Chem. Phys.* **119** 10015–10031

[140] Lhuillier C and Levesque D 1981 Three-body-correlation effect on the ground-state properties of ^{3}He and ^{3}He↑ *Phys. Rev. B* **23** 2203–2208

[141] Schmidt K E, Lee M A, Kalos M H and Chester G V 1981 Structure of the ground state of a fermion fluid *Phys. Rev. Lett.* **47** 807–810

[142] Kwon Y, Ceperley D M and Martin R M 1993 Effects of three-body and backflow correlations in the

two-dimensional electron gas *Phys. Rev. B* **48** 12037–12046

[143] Kwon Y, Ceperley D M and Martin R M 1998 Effects of backflow correlation in the three-dimensional electron gas: Quantum Monte Carlo study *Phys. Rev. B* **58** 6800–6806

[144] Holzmann M, Bernu B and Ceperley D M 2006 Many-body wavefunctions for normal liquid ^{3}He *Phys. Rev. B* **74** 104510

[145] Towler M D, Hood R Q and Needs R J 2000 Minimum principles and level splitting in quantum Monte Carlo excitation energies: Application to diamond *Phys. Rev. B* **62** 2330–2337

[146] Monkhorst H J and Pack J D 1976 Special points for Brillouin-zone integrations *Phys. Rev. B* **13** 5188–5192

[147] Filippi C and Umrigar C J 1996 Multiconfiguration wave functions for quantum Monte Carlo calculations of first-row diatomic molecules *J. Chem. Phys.* **105** 213–226

[148] Toulouse J and Umrigar C J 2008 Full optimization of Jastrow–Slater wave functions with application to the first-row atoms and homonuclear diatomic molecules *J. Chem. Phys.* **128** 174101

[149] Filippi C and Fahy S 2000 Optimal orbitals from energy fluctuations in correlated wave functions *J. Chem. Phys.* **112** 3523–3531

[150] Schautz F and Filippi C 2004 Optimized Jastrow–Slater wave functions for ground and excited states: Application to the lowest states of ethene *J. Chem. Phys.* **120** 10931–10941

[151] Umezawa N and Chikyow T 2006 Role of the one-body Jastrow factor in the transcorrelated self-consistent field equation *Int. J. Quant. Chem.* **106** 1477–1486

[152] Sakuma R and Tsuneyuki S 2006 Electronic structure calculations of solids with a similarity-transformed hamiltonian *J. Phys. Soc. Jpn.* **75** 103705

[153] Prasad R, Umezawa N, Domin D, Salomon-Ferrer R and Lester Jr W A 2007 Quantum Monte Carlo study of first-row atoms using transcorrelated variational Monte Carlo trial functions *J. Chem. Phys.* **126** 164109

[154] Wagner L and Mitas L 2003 A quantum Monte Carlo study of electron correlation in transition metal oxygen molecules *Chem. Phys. Lett.* **370** 412–417

[155] Wagner L K and Mitas L 2007 Energetics and dipole moment of transition metal monoxides by quantum Monte Carlo *J. Chem. Phys.* **126** 034105

[156] Sola E, Brodholt J P and Alfè D 2009 Equation of state of hexagonal closed packed iron under Earth's core conditions from quantum Monte Carlo calculations *Phys. Rev. B* **79** 024107

[157] Kolorenč J, Hu S and Mitas L 2010 Wave functions for quantum Monte Carlo calculations in solids: Orbitals from density functional theory with hybrid exchange-correlation functionals *Phys. Rev. B* **82** 115108

[158] Hernández E, Gillan M J and Goringe C M 1997 Basis functions for linear-scaling first-principles calculations *Phys. Rev. B* **55** 13485–13493

[159] Alfè D and Gillan M J 2004 Efficient localized basis set for quantum Monte Carlo calculations on condensed matter *Phys. Rev. B* **70** 161101

[160] Williamson A J, Hood R Q and Grossman J C 2001 Linear-scaling quantum Monte Carlo calculations *Phys. Rev. Lett.* **87** 246406

[161] Alfè D and Gillan M J 2004 Linear-scaling quantum Monte Carlo technique with non-orthogonal localized orbitals *J. Phys.: Condens. Matter* **16** L305–L311

[162] Reboredo F A and Williamson A J 2005 Optimized nonorthogonal localized orbitals for linear scaling quantum Monte Carlo calculations *Phys. Rev. B* **71** 121105(R)

[163] Bajdich M, Mitas L, Wagner L K and Schmidt K E 2008 Pfaffian pairing and backflow wavefunctions for electronic structure quantum Monte Carlo methods *Phys. Rev. B* **77** 115112

[164] Bardeen J, Cooper L N and Schrieffer J R 1957 Theory of superconductivity *Phys. Rev.* **108** 1175–1204

[165] Bouchaud J, Georges A and Lhuillier C 1988 Pair wave functions for strongly correlated fermions and their determinantal representation *J. Phys. France* **49** 553–559

[166] Carlson J, Chang S Y, Pandharipande V R and Schmidt K E 2003 Superfluid Fermi gases with large scattering length *Phys. Rev. Lett.* **91** 050401

[167] Giorgini S, Pitaevskii L P and Stringari S 2008 Theory of ultracold atomic Fermi gases *Rev. Mod. Phys.* **80** 1215–1274

[168] Casula M and Sorella S 2003 Geminal wave functions with Jastrow correlation: A first application to atoms *J. Chem. Phys.* **119** 6500–6511

[169] Casula M, Attaccalite C and Sorella S 2004 Correlated geminal wave function for molecules: An efficient resonating valence bond approach *J. Chem. Phys.* **121** 7110

[170] Bouchaud J P and Lhuillier C 1987 A new variational description of liquid ^{3}He: The superfluid glass *Europhys. Lett.* **3** 1273

[171] Bajdich M, Mitas L, Drobný G, Wagner L K and Schmidt K E 2006 Pfaffian pairing wave functions in electronic-structure quantum Monte Carlo simulations *Phys. Rev. Lett.* **96** 130201

[172] Feynman R P 1954 Atomic theory of the two-fluid model of liquid helium *Phys. Rev.* **94** 262–277

[173] Feynman R P and Cohen M 1956 Energy spectrum of the excitations in liquid helium *Phys. Rev.* **102** 1189–1204

[174] López Ríos P, Ma A, Drummond N D, Towler M D and Needs R J 2006 Inhomogeneous backflow transformations in quantum Monte Carlo calculations *Phys. Rev. E* **74** 066701

[175] Sugiyama G, Zerah G and Alder B J 1989 Ground-state properties of metallic lithium *Physica A* **156** 144–168

[176] Yao G, Xu J G and Wang X W 1996 Pseudopotential variational quantum Monte Carlo approach to bcc lithium *Phys. Rev. B* **54** 8393–8397

[177] Gaudoin R, Foulkes W M C and Rajagopal G 2002 Ab initio calculations of the cohesive energy and the bulk modulus of aluminium *J. Phys.: Condens. Matter* **14** 8787–8793

[178] Malatesta A, Fahy S and Bachelet G B 1997 Variational quantum Monte Carlo calculation of the cohesive properties of cubic boron nitride *Phys. Rev. B* **56** 12201–12210

[179] Knittle E, Wentzcovitch R M, Jeanloz R and Cohen M L 1989 Experimental and theoretical equation of state of cubic boron nitride *Nature* **337** 349 – 352

[180] Hood R Q, Kent P R C, Needs R J and Briddon P R 2003 Quantum Monte Carlo study of the optical and diffusive properties of the vacancy defect in diamond *Phys. Rev. Lett.* **91** 076403

[181] Yin M T and Cohen M L 1981 Ground-state properties of diamond *Phys. Rev. B* **24** 6121–6124

[182] Alfè D, Gillan M J, Towler M D and Needs R J 2004 Diamond and β-tin structures of Si studied with quantum Monte Carlo calculations *Phys. Rev. B* **70** 214102

[183] Farid B and Godby R W 1991 Cohesive energies of crystals *Phys. Rev. B* **43** 14248–14250

[184] Eckstein H, Schattke W, Reigrotzki M and Redmer R 1996 Variational quantum Monte Carlo ground state of GaAs *Phys. Rev. B* **54** 5512–5515

[185] Arthur J R 1967 Vapor pressures and phase equilibria in the Ga–As system *J. Phys. Chem. Solids* **28** 2257–2267

[186] Needs R J and Towler M D 2003 The diffusion quantum Monte Carlo method: Designing trial wave functions for NiO *Int. J. Mod. Phys. B* **17** 5425–5434

[187] Wagner L K 2007 Transition metal oxides using quantum Monte Carlo *J. Phys.: Condens. Matter* **19** 343201

[188] Linde D R, ed 2007 *CRC Handbook of Chemistry and Physics* (CRC Press/Taylor and Francis)

[189] Wigner E 1934 On the interaction of electrons in metals *Phys. Rev.* **46** 1002–1011

[190] Alder B J, Ceperley D M and Pollock E L 1982 Computer simulation of phase transitions in classical and quantum systems *Int. J. Quantum Chem.* **22** 49–61

[191] Ortiz G and Ballone P 1994 Correlation energy, structure factor, radial distribution function, and momentum distribution of the spin-polarized uniform electron gas *Phys. Rev. B* **50** 1391–1405

[192] Ortiz G, Harris M and Ballone P 1999 Zero temperature phases of the electron gas *Phys. Rev. Lett.* **82** 5317–5320

[193] Zong F H, Lin C and Ceperley D M 2002 Spin polarization of the low-density three-dimensional electron gas *Phys. Rev. E* **66** 036703

[194] Gurtubay I G, Gaudoin R and Pitarke J M 2010 Benchmark quantum Monte Carlo calculations of the ground-state kinetic, interaction and total energy of the three-dimensional electron gas *J. Phys.: Condens. Matter* **22** 065501

[195] Huotari S, Soininen J A, Pylkkänen T, Hämäläinen K, Issolah A, Titov A, McMinis J, Kim J, Esler K, Ceperley D M, Holzmann M and Olevano V 2010 Momentum distribution and renormalization factor in sodium and the electron gas *Phys. Rev. Lett.* **105** 086403

[196] Perdew J P and Wang Y 1992 Accurate and simple analytic representation of the electron-gas correlation energy *Phys. Rev. B* **45** 13244–13249

[197] Tanatar B and Ceperley D M 1989 Ground state of the two-dimensional electron gas *Phys. Rev. B* **39** 5005–5016

[198] Varsano D, Moroni S and Senatore G 2001 Spin-polarization transition in the two-dimensional electron gas *Europhys. Lett.* **53** 348–353

[199] Attaccalite C, Moroni S, Gori-Giorgi P and Bachelet G B 2002 Correlation energy and spin polarization in the 2D electron gas *Phys. Rev. Lett.* **88** 256601

[200] Drummond N D and Needs R J 2009 Quantum Monte Carlo study of the ground state of the two-dimensional Fermi fluid *Phys. Rev. B* **79** 085414

[201] Drummond N D and Needs R J 2009 Phase diagram of the low-density two-dimensional homogeneous electron gas *Phys. Rev. Lett.* **102** 126402

[202] Holzmann M, Bernu B, Olevano V, Martin R M and Ceperley D M 2009 Renormalization factor and effective mass of the two-dimensional electron gas *Phys. Rev. B* **79** 041308(R)

[203] Yoon J, Li C C, Shahar D, Tsui D C and Shayegan M 1999 Wigner crystallization and metal-insulator transition of two-dimensional holes in GaAs at b = 0 *Phys. Rev. Lett.* **82** 1744–1747

[204] Fahy S, Wang X W and Louie S G 1988 Variational quantum Monte Carlo nonlocal pseudopotential approach to solids: Cohesive and structural properties of diamond *Phys. Rev. Lett.* **61** 1631–1634

[205] Li X P, Ceperley D M and Martin R M 1991 Cohesive energy of silicon by the Green's-function Monte Carlo method *Phys. Rev. B* **44** 10929–10932

[206] Leung W K, Needs R J, Rajagopal G, Itoh S and Ihara S 1999 Calculations of silicon self-interstitial defects *Phys. Rev. Lett.* **83** 2351–2354

[207] Berliner R and Werner S A 1986 Effect of stacking faults on diffraction: The structure of lithium metal *Phys. Rev. B* **34** 3586–3603

[208] Felice R A, Trivisonno J and Schuele D E 1977 Temperature and pressure dependence of the single-crystal elastic constants of ^{6}Li and natural lithium *Phys. Rev. B* **16** 5173–5184

[209] Predel B 1998 *Landolt-Börnstein, Group IV Physical Chemistry – Phase Equilibria, Crystallographic and Thermodynamic Data of Binary Alloys, Volume 5 – Electronic Materials and Semiconductors* (Springer-Verlag Berlin)

[210] Cottam R I and Saunders G A 1973 The elastic constants of GaAs from 2 K to 320 K *J. Phys. C: Solid State Phys.* **6** 2105–2118

[211] Binnie S J, Sola E, Alfè D and Gillan M J 2009 Benchmarking DFT surface energies with quantum Monte Carlo *Molecular Simulation* **35** 609–612

[212] Loubeyre P, Toullec R L, Hanfland M, Ulivi L, Datchi F and Hausermann D 1998 Equation of state of ^{7}LiH and ^{7}LiD from x-ray diffraction to 94 GPa *Phys. Rev. B* **57** 10403–10406

[213] Datchi F, Dewaele A, Godec Y L and Loubeyre P 2007 Equation of state of cubic boron nitride at high pressures and temperatures *Phys. Rev. B* **75** 214104

[214] Walker C B and Marezio M 1959 Lattice parameters and zone overlap in solid solutions of lead in magnesium *Acta Metallurgica* **7** 769–773

[215] Errandonea D, Meng Y, Häusermann D and Uchida T 2003 Study of the phase transformations and equation of state of magnesium by synchrotron x-ray diffraction *J. Phys.: Condens. Matter* **15** 1277–1289

[216] Alfè D, Alfredsson M, Brodholt J, Gillan M J, Towler M D and Needs R J 2005 Quantum Monte Carlo calculations of the structural properties and the B1-B2 phase transition of MgO *Phys. Rev. B* **72** 014114

[217] Fei Y 1999 Effects of temperature and composition on the bulk modulus of (Mg,Fe)O *Am. Mineral.* **84** 272–276

[218] Bortz M, Bertheville B, Böttger G and Yvon K 1999 Structure of the high pressure phase γ-MgH_2 by neutron powder diffraction *J. Alloys Compd.* **287** L4–L6

[219] Maezono R, Ma A, Towler M D and Needs R J 2007 Equation of state and Raman frequency of diamond from quantum Monte Carlo simulations *Phys. Rev. Lett.* **98** 025701

[220] McSkimin H J and Andreatch Jr P 1972 Elastic moduli of diamond as a function of pressure and temperature *J. Appl. Phys.* **43** 2944–2948

[221] Okada Y and Tokumaru Y 1984 Precise determination of lattice parameter and thermal expansion coefficient of silicon between 300 and 1500 K *J. Appl. Phys.* **56** 314–320

[222] Hall J J 1967 Electronic effects in the elastic constants of n-type silicon *Phys. Rev.* **161** 756–761

[223] Driver K P, Cohen R E, Wu Z, Militzer B, López Ríos P, Towler M D, Needs R J and Wilkins J W 2010 Quantum Monte Carlo computations of phase stability, equations of state, and elasticity of high-pressure silica *PNAS* **107** 9519–9524

[224] Hazen R, Finger L, Hemley R and Mao H 1989 High-pressure crystal chemistry and amorphization of α-quartz *Solid State Commun.* **72** 507–511

[225] McCammon C A and Liu L 1984 The effects of pressure and temperature on nonstoichiometric wüstite, Fe_xO: The iron-rich phase boundary *Phys. Chem. Minerals* **10** 106–113

[226] Zhang J 2000 Effect of defects on the elastic properties of wüstite *Phys. Rev. Lett.* **84** 507–510

[227] Murnaghan F D 1944 The compressibility of media under extreme pressures *Proc. Natl. Acad. Sci. U.S.A.* **30** 244–247

[228] Vinet P, Ferrante J, Smith J R and Rose J H 1986 A universal equation of state for solids *J. Phys. C: Solid State Phys.* **19** L467–L473

[229] Drummond N D and Needs R J 2006 Quantum Monte Carlo, density functional theory, and pair potential studies of solid neon *Phys. Rev. B* **73** 024107

[230] Spanu L, Sorella S and Galli G 2009 Nature and strength of interlayer binding in graphite *Phys. Rev. Lett.* **103** 196401

[231] Drummond N D and Needs R J 2007 van der Waals interactions between thin metallic wires and layers *Phys. Rev. Lett.* **99** 166401

[232] Hamann D R 1996 Generalized gradient theory for silica phase transitions *Phys. Rev. Lett.* **76** 660–663

[233] Purwanto W, Krakauer H and Zhang S 2009 Pressure-induced diamond to β-tin transition in bulk silicon: A quantum Monte Carlo study *Phys. Rev. B* **80** 214116

[234] Jeanloz R and Ahrens T J 1980 Equations of state of FeO and CaO *Geophys. J. Int.* **62** 505–528

[235] Fei Y and Mao H 1994 In situ determination of the NiAs phase of FeO at high pressure and temperature *Science* **266** 1678–1680

[236] Grossman J C and Mitas L 2005 Efficient quantum Monte Carlo energies for molecular dynamics simulations *Phys. Rev. Lett.* **94** 056403

[237] Sola E and Alfè D 2009 Melting of iron under Earth's core conditions from diffusion Monte Carlo free energy calculations *Phys. Rev. Lett.* **103** 078501

[238] Batista E R, Heyd J, Hennig R G, Uberuaga B P, Martin R L, Scuseria G E, Umrigar C J and Wilkins J W 2006 Comparison of screened hybrid density functional theory to diffusion Monte Carlo in calculations of total energies of silicon phases and defects *Phys. Rev. B* **74** 121102(R)

[239] Alfè D and Gillan M J 2005 Schottky defect forma-

tion energy in MgO calculated by diffusion Monte Carlo *Phys. Rev. B* **71** 220101

[240] Leslie M and Gillan M J 1985 The energy and elastic dipole tensor of defects in ionic crystals calculated by the supercell method *J. Phys. C: Solid State Phys.* **18** 973–982

[241] Makov G and Payne M C 1995 Periodic boundary conditions in ab initio calculations *Phys. Rev. B* **51** 4014–4022

[242] Wood B, Hine N D M, Foulkes W M C and García-González P 2007 Quantum Monte Carlo calculations of the surface energy of an electron gas *Phys. Rev. B* **76** 035403

[243] Acioli P H and Ceperley D M 1996 Diffusion Monte Carlo study of jellium surfaces: Electronic densities and pair correlation functions *Phys. Rev. B* **54** 17199–17207

[244] Healy S B, Filippi C, Kratzer P, Penev E and Scheffler M 2001 Role of electronic correlation in the Si(100) reconstruction: A quantum Monte Carlo study *Phys. Rev. Lett.* **87** 016105

[245] Bokes P, Štich I and Mitas L 2002 Ground-state reconstruction of the Si(001) surface: symmetric versus buckled dimers *Chem. Phys. Lett.* **362** 559–566

[246] Lampart W M, Schofield D P, Christie R A and Jordan K D 2008 Model systems for exploring electron correlation effects in the buckling of SiSi dimers on the Si(100) surface *Molecular Physics* **106** 1697–1702

[247] Alfè D and Gillan M J 2006 The energetics of oxide surfaces by quantum Monte Carlo *J. Phys.: Condens. Matter* **18** L435–L440

[248] Mitas L and Kolorenč J 2010 Quantum Monte Carlo studies of transition metal oxides *Rev. Mineral. Geochem.* **71** 137–145

[249] van Elp J, Potze R H, Eskes H, Berger R and Sawatzky G A 1991 Electronic structure of MnO *Phys. Rev. B* **44** 1530–1537

[250] Bowen H K, Adler D and Auker B H 1975 Electrical and optical properties of FeO *J. Solid State Chem.* **12** 355–359

[251] Mitáš L and Martin R M 1994 Quantum Monte Carlo of nitrogen: Atom, dimer, atomic, and molecular solids *Phys. Rev. Lett.* **72** 2438–2441

[252] Williamson A J, Hood R Q, Needs R J and Rajagopal G 1998 Diffusion quantum Monte Carlo calculations of the excited states of silicon *Phys. Rev. B* **57** 12140–12144

[253] Mitas L 1996 Electronic structure by quantum Monte Carlo: atoms, molecules and solids *Comput. Phys. Commun.* **96** 107–117

[254] Khairallah S A and Militzer B 2008 First-principles studies of the metallization and the equation of state of solid helium *Phys. Rev. Lett.* **101** 106407

[255] Bajdich M, Kolorenč J, Mitas L and Reynolds P J 2010 Pairing in cold atoms and other applications for quantum Monte Carlo methods *Physics Procedia* **3** 1397–1410

[256] Eagles D M 1969 Possible pairing without superconductivity at low carrier concentrations in bulk and thin-film superconducting semiconductors *Phys. Rev.* **186** 456–463

[257] Leggett A J 1980 Cooper pairing in spin-polarized Fermi systems *J. Phys. Colloques* **41** C7–19–C7–26

[258] Nozières P and Schmitt-Rink S 1985 Bose condensation in an attractive fermion gas: From weak to strong coupling superconductivity *J. Low Temp. Phys.* **59** 195–211

[259] Ketterle W and Zwierlein M W 2008 Making, probing and understanding ultracold Fermi gases *Rivista del Nuovo Cimento* **31** 247–422

[260] Astrakharchik G E, Boronat J, Casulleras J and Giorgini S 2004 Equation of state of a Fermi gas in the BEC-BCS crossover: A quantum Monte Carlo study *Phys. Rev. Lett.* **93** 200404

[261] Chang S Y, Pandharipande V R, Carlson J and Schmidt K E 2004 Quantum Monte Carlo studies of superfluid Fermi gases *Phys. Rev. A* **70** 043602

[262] Morris A J, López Ríos P and Needs R J 2010 Ultracold atoms at unitarity within quantum Monte Carlo methods *Phys. Rev. A* **81** 033619

[263] Yang C N 1962 Concept of off-diagonal long-range order and the quantum phases of liquid He and of superconductors *Rev. Mod. Phys.* **34** 694–704

[264] De Palo S, Rapisarda F and Senatore G 2002 Excitonic condensation in a symmetric electron-hole bilayer *Phys. Rev. Lett.* **88** 206401

[265] Astrakharchik G E, Boronat J, Casulleras J and Giorgini S 2005 Momentum distribution and condensate fraction of a fermion gas in the BCS-BEC crossover *Phys. Rev. Lett.* **95** 230405

[266] Chang S Y and Bertsch G F 2007 Unitary Fermi gas in a harmonic trap *Phys. Rev. A* **76** 021603(R)

[267] Blume D, von Stecher J and Greene C H 2007 Universal properties of a trapped two-component Fermi gas at unitarity *Phys. Rev. Lett.* **99** 233201

[268] von Stecher J, Greene C H and Blume D 2008 Energetics and structural properties of trapped two-component Fermi gases *Phys. Rev. A* **77** 043619

[269] Salasnich L and Toigo F 2008 Extended Thomas–Fermi density functional for the unitary Fermi gas *Phys. Rev. A* **78** 053626